Journal of Alloys and Compounds 977 (2024) 173418

Contents lists available at ScienceDirect

Journal of Alloys and Compounds

journal homepage: www.elsevier.com/locate/jalcom

Y effects on the Cu-Zr-Fe alloys' aging behavior and properties

Mixue Guo [a], Meng Zhou [a], Jin Zou [b,*], Ke Jing [a], Haoyan Hu [a], Yi Zhang [a,*], Qian Bai [c], Caijiao Tian [a], Baohong Tian [a], Xu Li [d], Alex A. Volinsky [e]

[a] School of Materials Science and Engineering, Henan University of Science and Technology, Provincial and Ministerial Co-construction of Collaborative Innovation Center for Non-ferrous Metals New Materials and Advanced Processing Technology, Luoyang 471023, PR China
[b] Jiangxi Key Laboratory for Advanced Copper and Tungsten Materials, Jiangxi Academic of Sciences, Nanchang 330096, PR China
[c] Medical Research Center, The Second Affiliated Hospital of Zhengzhou University, Zhengzhou 450014, PR China
[d] Center for Advanced Measurement Science, National Institute of Metrology, Beijing 100029, PR China
[e] Department of Mechanical Engineering, University of South Florida, 4202 E. Fowler Ave. ENG 030, Tampa 33620, USA

ARTICLE INFO

Keywords:
Cu-Zr-Fe(-Y) alloy
Precipitated phases
Properties
Microstructure evolution
Recrystallization

ABSTRACT

Cu-Zr-Fe(-Y) alloys were prepared by vacuum melting, and their microstructure, elemental distribution and mechanical properties were analyzed. The microstructure evolution, dislocation morphology and precipitated phase distribution due to aging were investigated by electron backscatter diffraction and transmission electron microscopy. The optimal process parameters for the Cu-Zr-Fe(-Y) alloy after solution treatment at 930 °C with 60% cold rolling are 450 °C aging for 120 min and 500 °C aging for 20 min, resulting in microhardness, electrical conductivity, and tensile strength of 60.9% IACS, 162.4 HV, 512.8 MPa and 54.8% IACS, 177.7 HV, 546.9 MPa, respectively. The addition of Y has a fine grain strengthening effect, resulting in an increase in hardness and strength by 9.4% and 6.6%, respectively. The precipitated Cu_5Zr and γ-Fe phases pinned the dislocations and played a significant role in the aging hardening of the alloy, being the main contributors to the strengthening effects.

1. Introduction

Copper alloys play a crucial role in many industries due to their excellent properties, including corrosion resistance and high electrical conductivity, so they are widely used as electrical connectors, electronic products, instruments, in aerospace and other fields [1–5]. Among them, Cu-Zr alloy has been extensively studied due to its excellent creep resistance, high thermal and electrical conductivity, and heat resistance [6,7]. Cu-Zr is an age-hardened alloy, and its excellent electrical conductivity is attributed to the extremely low solubility of Zr in the copper matrix at room temperature, which rapidly decreases with decreasing temperature [8]. The higher strength is due to the dispersion-strengthening effect of the precipitated Cu_xZr compounds inhibiting dislocation movement during the aging process [9]. For example, Zhang et al. [10] studied the microstructure of the Cu-Cr-Zr-Ce alloy after aging at 400 °C for 8 h by high-resolution transmission electron microscopy (HRTEM), which showed that the alloy was aged. A rod-shaped Cr-rich phase and a face-centered cubic (fcc) Cu_4Zr precipitated phase were found. The fcc precipitated phase was co-compacted with the Cu matrix, causing lattice strengthening. Wang et al. [11] studied the properties of Cu-Cr-Zr alloys under different aging conditions and observed two chromium-rich precipitated phases with face-centered cubic and body-centered cubic structures, and two Cu_4Zr and Cu_5Zr zirconium-rich precipitation phases by transmission electron microscopy (TEM) and HRTEM.

The strength and electrical conductivity of Cu-Zr alloys are closely related to the size, type, and distribution of the precipitates. Therefore, by employing appropriate heat treatment processes or microalloying, the distribution of precipitates can be controlled to achieve the optimal comprehensive performance of the alloy. For example, Krishna et al. [12] studied the properties of Cu-Ag-Zr alloys under different degrees of cold rolling, and the alloy has the highest strength after 80% cold rolling and 400 °C aging for 1 h, with the yield and ultimate tensile strength of 511 MPa and 560 MPa, respectively, and 12% ductility. Fu et al. [13] explored the properties of aged Cu-Cr-Ti alloy and found that the alloy has better overall properties after 80% cold rolling and 500 °C aging for 1 h with microhardness, tensile strength, and electrical conductivity of 166 HV, 551 MPa, and 78.2% IACS, respectively.

---

* Corresponding authors.
E-mail addresses: niatzou@126.com (J. Zou), zhshgu436@163.com (Y. Zhang).

https://doi.org/10.1016/j.jallcom.2024.173418
Received 6 November 2023; Received in revised form 19 December 2023; Accepted 1 January 2024

In addition, according to previous studies that the role of precipitation-strengthened Fe elements in alloying elements is to form diffuse fine Fe phases to strengthen the matrix[14], the combination of two precipitation-strengthened elements, Fe and Zr, in a copper base has been the subject of a small number of studies in the past, such as Yang et al.[15] through the calculation of the phase diagram to prepare a new precipitation-strengthened Cu-0.18Fe-0.10Zr alloy, with the following characteristics. After solid solution water quenching treatment at 950 °C for 12 h and cold rolling treatment at 0%, 40%, 60%, 80% and 90%, the alloy was subjected to aging treatment at aging temperatures of 450 °C-500 °C for different aging times. The results show that the alloy has good comprehensive performance after 90% cold rolling and aging at 450 °C for 1 h, at this time, the hardness, electrical conductivity, tensile strength of 165 HV, 72% IACS and 515 MPa, respectively, at the same time, the two coherent with the substrate Fe phase, Fe_2Zr phase precipitation in this aging conditions, the presence of two precipitated phases have a significant impact on the improvement of the alloy in terms of hardness and electrical conductivity. Nevertheless, the current research on the preparation of high content Cu-Zr-Fe alloys by microalloying method is minimal.

It is well known that rare earth elements are chemically active and exhibit metallic properties [16,17]. Currently, a large number of studies have found that adding appropriate amounts of rare earth elements to copper alloys can optimize their comprehensive performance and refine the microstructure. For example, Wang et al. [18] analyzed the role of trace La element in the Cu-0.2Zr alloy for the heat treatment process. The addition of La refined the alloy grain, and increased the alloy hardness and strength by 3% and 4.5%, respectively, without significantly reducing its electrical conductivity. Li et al. [19] investigated the effects of adding small amounts of rare earth Ce element on the microstructure and properties of cast pure copper. Ce refined the grain sizes of cast pure copper, and the alloy achieved a maximum tensile strength of 182 MPa with the addition of 0.12 wt% Ce.

In this paper, rare earth element Y is combined with high content Cu-Zr-Fe alloy to prepare a new copper alloy for in-depth study. The microstructure, electrical and mechanical properties of Cu-Zr-Fe-(Y) alloys under 0% and 60% cold deformation, and different aging conditions were investigated. The effects of Y on the microstructure evolution due to aging was investigated by electron backscatter diffraction (EBSD). The morphology of dislocations, types, and distribution of precipitates in the alloy after aging were observed using transmission electron microscopy to study the strengthening mechanisms.

2. Experimental procedures

The experimental Cu-Zr-Fe(-Y) alloys were vacuum melted in a ZG-0.01–40-4 melting furnace at 1100–1200 °C. The raw materials for the experiments were: standard copper cathode Cu-CATH-1 with 99.95% purity, Cu-10%Zr intermediate alloy, and Cu-10%Fe intermediate alloy. The nominal and actual composition of the alloys is listed in Table 1.

The alloy ingots were homogenized at 850 °C 1 h, forged into ϕ40 mm cylinders and then machined into 135 mm × 10 mm× 2 mm samples, followed by 930 °C water quenching solution treatment for 1 h with Ar gas protection. The samples after solid solution treatment were cold deformed by 0% and 60%, respectively, and then the cold rolled samples were cut into 12 mm × 10 mm slices for aging treatment at 400 °C, 450 °C, 500 °C and 550 °C for 10–480 min. The whole process was protected by argon gas. The specific aging treatment process flow is shown in Fig. 1.

Table 1
Chemical composition of the Cu-Zr-Fe-(Y) alloys.

Alloy	Analyzed composition in wt%			
	Zr	Fe	Y	Cu
Cu-0.6Zr-0.3Fe	0.5201	0.2952	0	Bal.
Cu-0.6Zr-0.3Fe-0.15Y	0.5903	0.2835	0.1563	Bal.

The HVS-1000 microhardness tester was used to measure the hardness of the alloy according to the GB/T 4340–2009 standard. A Sigma2008 digital eddy current metal conductivity meter was used to measure the electrical conductivity of the alloy according to the GB/T 351–2019 standard. Each sample was tested three times, and the average value was reported. CMT450 microcomputer-controlled electronic universal tensile testing machine was used to test the specimens with the non-standard geometry shown in Fig. 2. The physical phase analysis of the solid solution alloy was carried out by X-ray diffraction (XRD, D8 ADVANCE), and the microstructure, fracture morphology, as well as elemental distribution of the alloy, were observed by optical microscopy (OM, CX40M), field-emission scanning electron microscopy (FESEM, JSM-7800 F), and energy dispersive spectrometry (EDS). The specimens were also characterized by EBSD and TEM to analyze the microstructure evolution, dislocation morphology and precipitated phases of the alloy after aging. The EBSD specimens were finely ground first, mechanically polished, and then electrolytically polished for 1 min. The electrolyte was a mix of 50% alcohol and 50% phosphoric acid with a 1:1 ratio, followed by 5 min of ultrasonic cleaning to prevent oxidation. The samples were observed by FESEM operated at 20 kV with a 2.5 μm step size. The TEM specimens were selected from the samples processed under optimal aging conditions. The specimens were first processed from rough to fine grinding below 70 μm, and then the TEM specimens were obtained by punching out the ϕ 3 mm discs in the appropriate position on the samples and thinning them using the ion milling apparatus (Gatan 69).

3. Results and discussion

3.1. Solid solution microstructure and properties

Fig. 3(a, b) show the microstructure of the Cu-Zr-Fe(-Y) alloy after solid solution treatment at 930 °C for 60 min. It is observed that there are some black dot-like eutectic phases between grains with spherical characteristics due to the large surface tension, accompanied by a large number of annealed twins, as pointed by arrows in Fig. 3. The twins contribute to the improvement of the alloy's plasticity and twin boundaries can hinder dislocations [20,21]. It is evident by comparing Fig. 3(a) with Fig. 3(b) that Y addition refines the reticulation substructure and the eutectic. On the one hand, this is due to the larger Y radius than Cu, Fe, and Zr, and a large number of vacancies may be generated due to the movement of Y during high-temperature crystallization, making it easier for solute atoms to dissolve and facilitating the formation of eutectic structure. On the other hand, since rare earth elements have limited solubility in copper, Y can easily enrich the solid-liquid interface front, which will lead to an increase in the degree of supercooling and accelerated nucleation rate, resulting in finer substructure [22]. Fig. 3(c) shows the hardness and electrical conductivity of the alloys in the solid solution state. The hardness and electrical conductivity of the Cu-Zr-Fe-Y alloy is higher than the Cu-Zr-Fe alloy, which originates from the fine grain strengthening of Y and the purifying effect of Y on the matrix.

In order to elucidate the composition of the solid solution eutectic, SEM and EDS analysis of the solid solution-treated Cu-Zr-Fe(-Y) alloys was carried out in Figs. 4 and 5. There are banded alloy phases in the matrix of both alloys, and the specimens were further characterized by EDS surface scanning and point analysis. The distribution of Cu, Fe, and Y elements is relatively homogeneous in the Cu matrix, but there are Zr-rich phases in the region of banded alloy phases. This is because Zr has limited solubility in the Cu matrix, and according to the Cu-Zr phase diagram [8], the solid solubility of Zr in the Cu matrix at the eutectic temperature of 967 °C is 0.15 wt%. Zr is not completely dissolved since the amount of Zr added to this alloy is much higher than its maximum solubility. In addition, according to the EDS results, there was less Fe

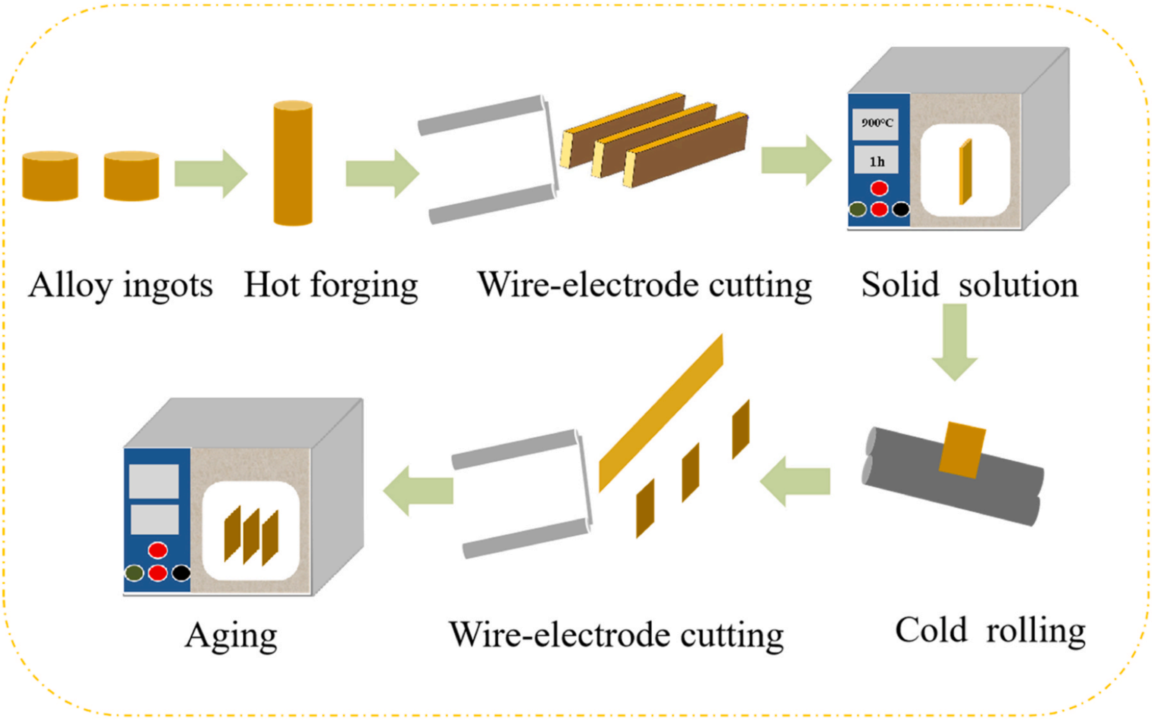

Fig. 1. The flow chart of aging treatment.

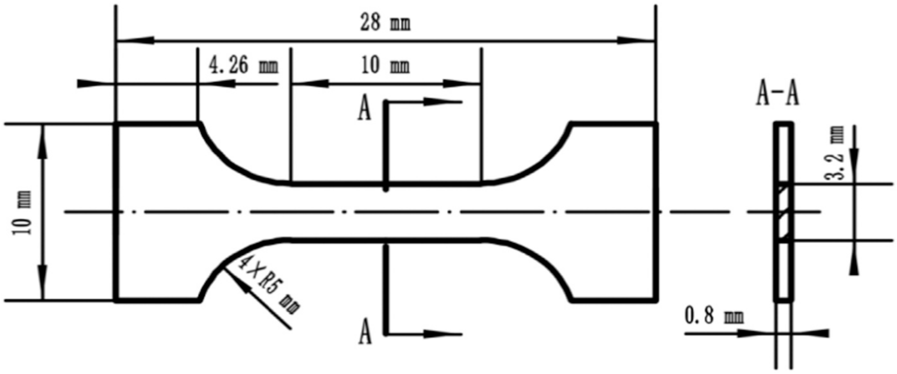

Fig. 2. Dimensions of the tensile specimen.

precipitation, and judged by the Cu-Zr atomic ratio, Cu-Zr compounds were also present in the strip alloy phase.

Fig. 6 shows the XRD patterns of the solid solution Cu-Zr-Fe(-Y) alloy. Although there is only Cu phase X-ray reflection after the solid solution treatment, the diffraction angle is slightly shifted to the higher diffraction angle compared to pure Cu. The lattice constant of the Cu-Zr-Fe(-Y) alloy was calculated using Bragg's law:

$$2d\sin\theta = n\lambda \tag{1}$$

Here, d is the crystal plane spacing, θ is the diffraction angle, n is the number of diffracting planes, and λ is the wavelength ($\lambda = 0.154$ nm). The crystal plane spacing of the alloy can be calculated from Eq. (1), and then according to the relationship between the crystal plane spacing and the lattice constant in the fcc structure, the lattice constant of the alloy is calculated as:

$$a = \mathrm{d} \times \sqrt{h^2 + k^2 + l^2} \tag{2}$$

Here, a is the lattice constant and h, k, l are the crystallographic indices.

Taking the (111) diffraction reflection as an example, combining the two equations yields the results in Table 2, which shows that the lattice constant of the alloy changes with the solidification process, producing a lattice distortion, which illustrates the significant solidification effect of the solute atoms in the Cu matrix.

3.2. Aged state properties

After solid solution treatment, cold deformation treatment of the alloy before aging can lead to higher electrical and mechanical properties [23–25]. Moreover, dislocations and other defects introduced during cold deformation avoid the agglomeration of precipitated phases at grain boundaries during the subsequent aging process, resulting in a more homogeneous distribution of the diffuse and fine precipitated phases [26]. Fig. 7 shows the microhardness of the Cu-Zr-Fe(-Y) alloy under different deformation and aging conditions. At the early aging stage, the microhardness rises rapidly to the peak value, then decreases with aging time, and finally tends to be flat or decreases at the last stage. This is mainly due to the high content of solid solution atoms in the matrix at the beginning of aging, and the excessive saturation with precipitation of a large number of secondary phase particles, which

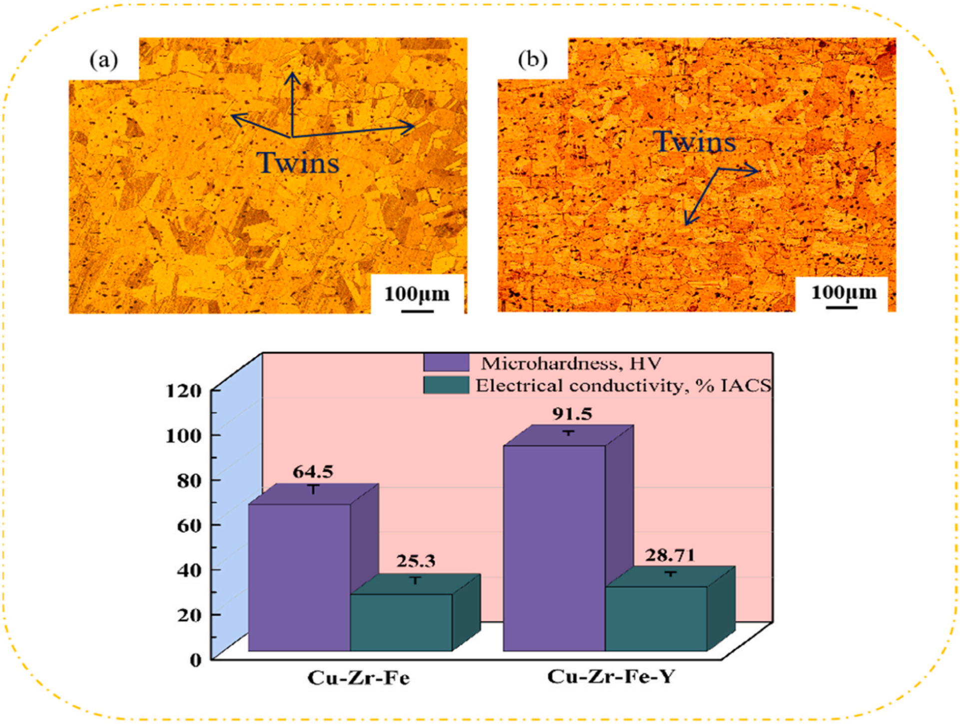

Fig. 3. Microstructure and properties of solid solution alloys: (a) Cu-Zr-Fe alloy. (b) Cu-Zr-Fe-Y alloy; (c) microhardness and electrical conductivity the Cu-Zr-Fe (-Y) alloy.

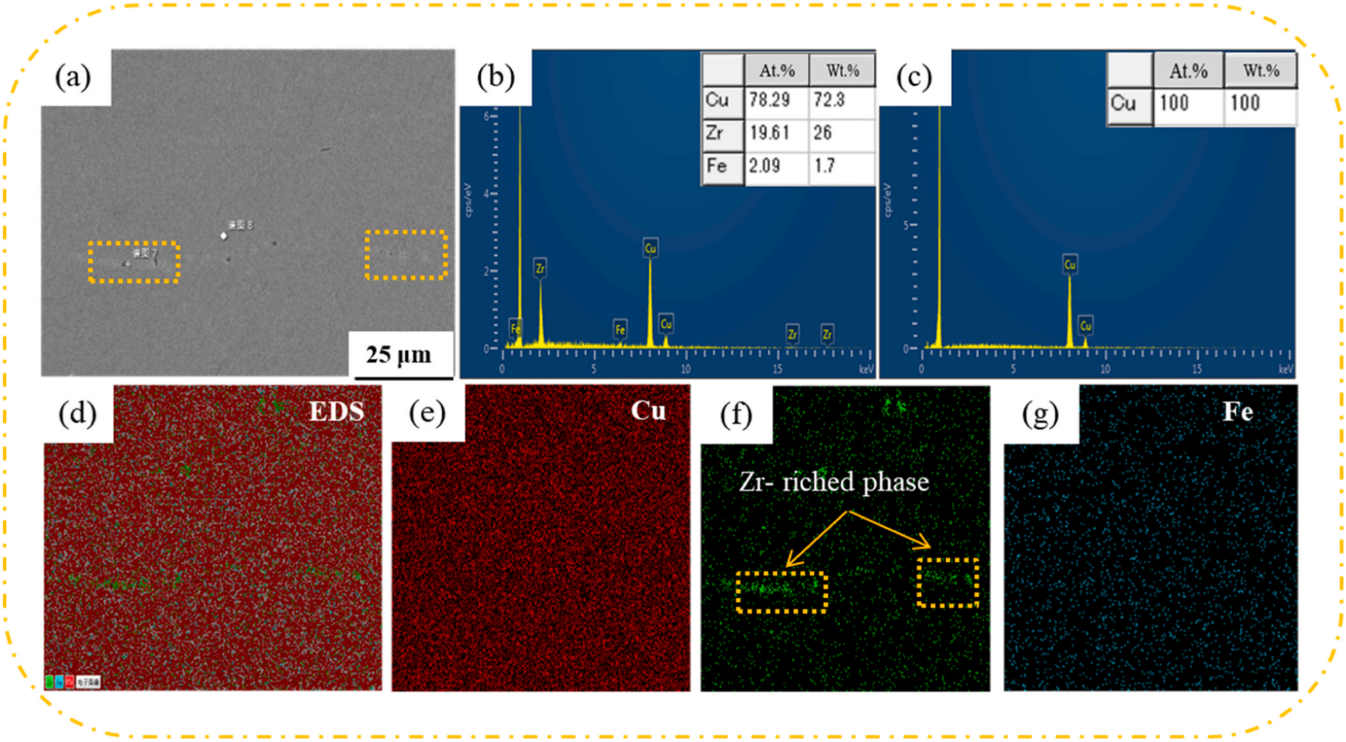

	At.%	Wt.%
Cu	78.29	72.3
Zr	19.61	26
Fe	2.09	1.7

	At.%	Wt.%
Cu	100	100

Fig. 4. SEM and EDS analysis of Cu-Zr-Fe alloys: (a) SEM image; (b, c) EDS point scans; (d) EDS combined map; (e) Cu; (f) Zr; (g) Fe elemental maps.

hinder dislocation motion and significantly strengthen the alloy [27–29]. However, over-aging occurs with prolonged aging when the precipitated phase grows and coarsens, deteriorating the mechanical properties [30,31]. Without cold deformation, the microhardness of Cu-Zr-Fe alloys aged at 400 °C and Cu-Zr-Fe-Y alloys aged at 400 °C and 450 °C tends to slowly increase, caused by the low aging temperature and small precipitation power, unfavorable to the diffusion of the solute atoms, along with slow and relatively stable precipitation of the secondary phase.

The time for alloys with different degrees of deformation to reach their peak hardness decreases with temperature and deformation, and the peak hardness increases with deformation. At 0% deformation in

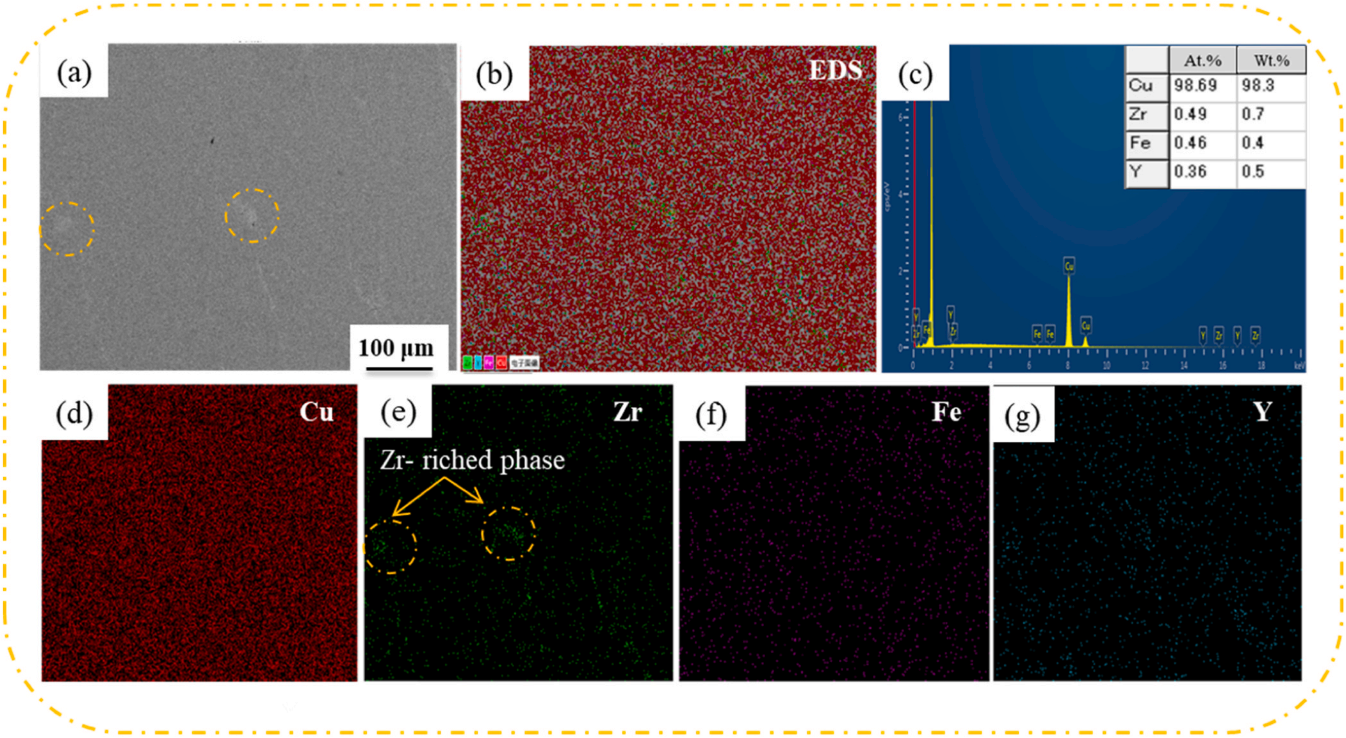

	At.%	Wt.%
Cu	98.69	98.3
Zr	0.49	0.7
Fe	0.46	0.4
Y	0.36	0.5

Fig. 5. SEM and EDS analysis of the Cu-Zr-Fe-Y alloy: (a) SEM image; (b) EDS combined map; (c) elemental content; (d) Cu; (e) Zr; (f) Fe; (g) Y elemental maps.

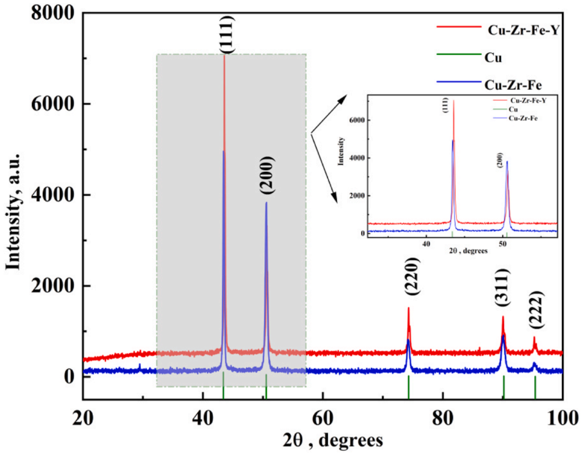

Fig. 6. XRD patterns of solid solution Cu-Zr-Fe(-Y) alloy.

Table 2
Lattice constants of alloys.

Alloy	Cu-rich phase diffraction reflections	d, Å	a, Å
Cu	(111)	2.09 (± 0.005)	3.61 (± 0.002)
Cu-Zr-Fe	(111)	2.08 (± 0.006)	3.60 (± 0.002)
Cu-Zr-Fe-Y	(111)	2.07 (± 0.001)	3.59 (± 0.001)

Fig. 7(a), the time to reach the peak microhardness of the Cu-Zr-Fe alloy aged at 450 °C, 500 °C, and 550 °C is 240 min, 60 min, and 20 min, corresponding to the peak hardness of 105 HV, 100 HV, and 99.2 HV, respectively. At 60% deformation, the time to peak hardness when aged at 450 °C, 500 °C, and 550 °C was 120 min, 20 min, and 10 min, corresponding to peak hardness of 162.4 HV, 156 HV, and 142.3 HV, respectively. The higher the temperature, the faster the decomposition of the supersaturated solid solution, the stronger the diffusion capacity of the atoms, and the greater the precipitation power to reach the peak hardness, and the shorter the aging time. Moreover, the alloy in the cold deformed state will produce dislocations and other defects in an effort to reduce the energy of the system dislocations in the form of slippage, climbing shift, etc. to form two-dimensional and three-dimensional dislocation network structures, which provide channels for the diffusion of the solute atoms to accelerate the secondary phases precipitation. Besides, large cold deformation increases the defect density, as precipitated phases and dislocations are prone to interact, increasing the resistance to dislocations movement [32] with high-density dislocations and excess solid solution atoms formed by the Kirchhoff's gas cluster also playing a role in pinning dislocations, and thus strengthening the matrix [33].

Comparison of Fig. 7(b) and Fig. 7(d) shows that the Cu-Zr-Fe(-Y) alloys deformed by 60% reached the peak microhardness of 162.4 HV and 177.7 HV after aging at 450 °C for 120 min and at 500 °C for 20 min, respectively. The Y addition significantly increased the hardness of the alloys, which is attributed to Y refining the grain, enlarging the area of grain boundaries, and enhancing the hindering effect on dislocations, which increased the microhardness of the alloys [34]. Y promoted the secondary precipitation phases and pinned dislocations during the aging process, which resulted in a more significant effect of precipitation reinforcement, and contributed to higher hardness [35].

Fig. 8 shows the electrical conductivity of the Cu-Zr-Fe(-Y) alloys under different cold deformation and aging conditions. The conductivity increased rapidly at the beginning of aging and leveled off or increased slowly as aging progressed. At the beginning of aging, the matrix has a high degree of supersaturation, the precipitation power is high, and the secondary phase will precipitate rapidly out of the matrix, reducing the effects of electron scattering, and thus rapidly increasing electrical conductivity [36]. The concentration of solute atoms within the matrix decreases and precipitation is weaker with continued aging and no significant conductivity change. Additionally, the conductivity of the

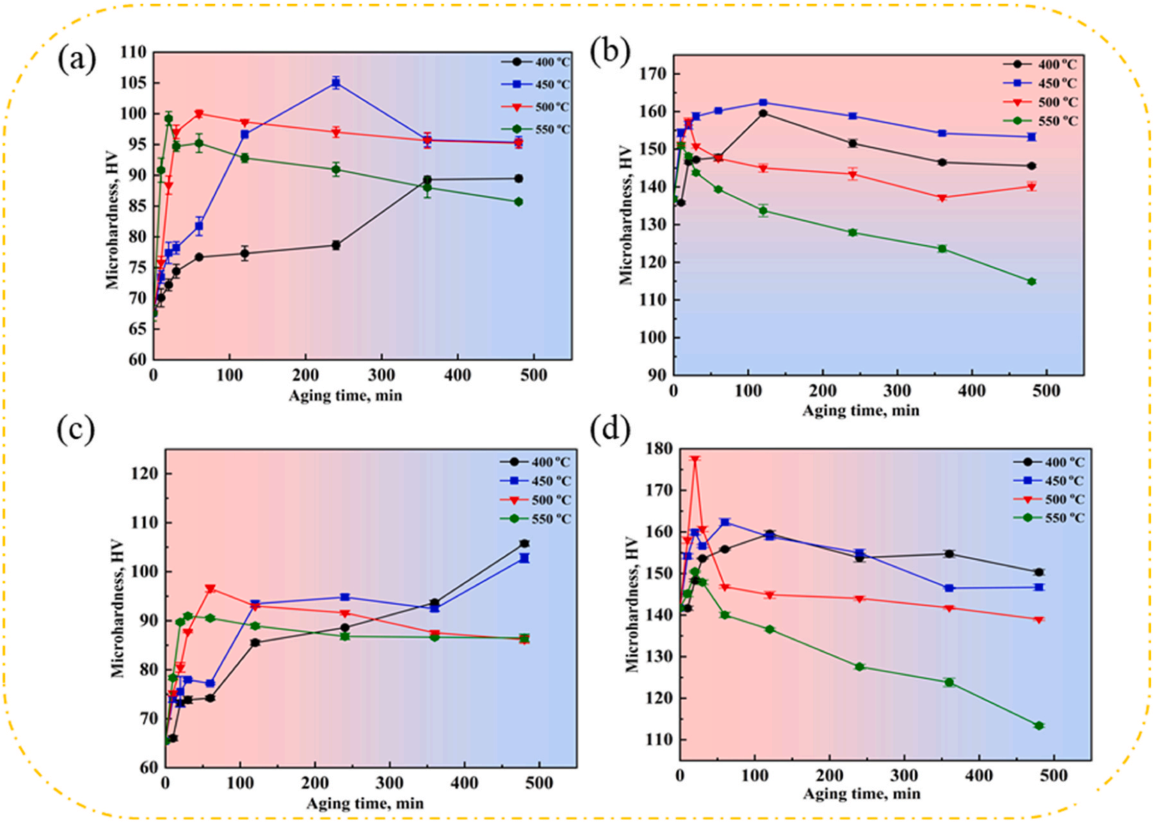

Fig. 7. Microhardness of the Cu-Zr-Fe(-Y) alloys under different deformations and aging conditions: (a) Cu-Zr-Fe alloy at 0% cold deformation; (b) Cu-Zr-Fe alloy at 60% cold deformation; (c) Cu-Zr-Fe-Y alloy at 0% cold deformation; (d) Cu-Zr-Fe-Y alloy at 60% cold deformation.

two alloys aged at 400 °C and 450 °C continue to increases due to the slower precipitation rate at lower temperatures.

In Fig. 8 the electrical conductivity increases with temperature for both deformations because the speed of vacancies generated by cold deformation will be faster, which increases the diffusion rate of solute atoms, favorable for the rapid purification of the matrix, weakening the scattering effects of solute atoms on the matrix, and thus accelerating the rate of electrical conductivity increase [37–40]. In Figs. 8(b) and 8(d) the electrical conductivity of the Cu-Zr-Fe(-Y) alloys at 60% deformation is 60.9% IACS and 54.8% IACS for the aging parameters corresponding to the peak hardness. The small decrease in the electrical conductivity by the addition of Y may be attributed to the fact that the rare earth elements purify the matrix while promoting the precipitated phases, which pinned dislocations to the extent that more dislocations are retained in the matrix, leading to a decrease in the electrical conductivity [41,42]. Therefore, the optimal aging parameters for the Cu-Zr-Fe(-Y) alloys were obtained from the comprehensive analysis as 120 min aging at 450 °C and 20 min aging at 500 °C, respectively.

The mechanical properties of the two Cu-Zr-Fe(-Y) alloys aged at respective peak hardness temperatures for different times were also investigated, listed in Table 3 and Table 4. The Cu-Zr-Fe(-Y) alloys reached the maximum tensile strength at peak hardness aging conditions of 512.8 MPa and 546.9 MPa. A comparison of the tensile strengths of the two alloys showed that the addition of Y increased the strength by 6.6%. Therefore, a comprehensive analysis concludes that Y significantly improves the microhardness and strength of the alloys and optimizes their overall properties.

Table 5 further compares the tensile strength and electrical conductivity of Cu-Zr-Fe(-Y) alloy with that of conventional copper alloys [43–49]. It can be observed that the addition of Fe and Y elements significantly improves the properties of Cu-Zr alloys, albeit at the cost of a reduction in electrical conductivity. In contrast, Y seems to have a more pronounced effect on the electrical conductivity, which may stem from the fact that although rare earths have the role of purifying the matrix, but in the aging process Y plays a role in promoting the precipitation of precipitated phases precipitation and grain refinement is much greater than the former, which makes the matrix in the grain boundaries increase, increasing the scattering effect on the electrons, which in turn reduces the alloy conductivity. Therefore, it can be concluded from Table 5 that Cu-Zr-Fe(-Y) alloys have good comprehensive properties.

Fig. 9 shows the tensile fracture morphology of the two Cu-Zr-Fe(-Y) alloys at their respective peak aging temperatures. The two alloys have larger, deeper, and more uniform tough nest sizes in the under-aged stage, which is typical of ductile fracture morphology, at which time the alloys have excellent plasticity, as shown by the yellow arrows in Fig. 9(a, d). In addition, the plasticity of the alloy is slightly restored by cold rolling[50], and as aging proceeds, the appearance of serpentine slip lines on the walls of the surrounding ligament fossa is observed, which are indicative of the characteristics of toughness fracture of the alloy, as shown by red arrows in Fig. 9(b, e). The presence of precipitation phases or impurity particles was also observed in the depth of some toughness nests, such as the circled areas in Fig. 9(b, f). These particles play an important role in the toughness nest fracture because when fracture occurs at high temperatures, cracks sprout around the particles and form smaller microporous holes. The molding principle of toughness nests lies in the aggregation of voids, which grow and aggregate under the action of the slip, forming toughness nests [51]. The comprehensive tensile fracture analysis of the Cu-Zr-Fe(-Y) demonstrates tough fracture, indicating that the alloy has good plasticity.

3.3. Aged microstructure analysis

It is concluded that Y addition significantly improves the

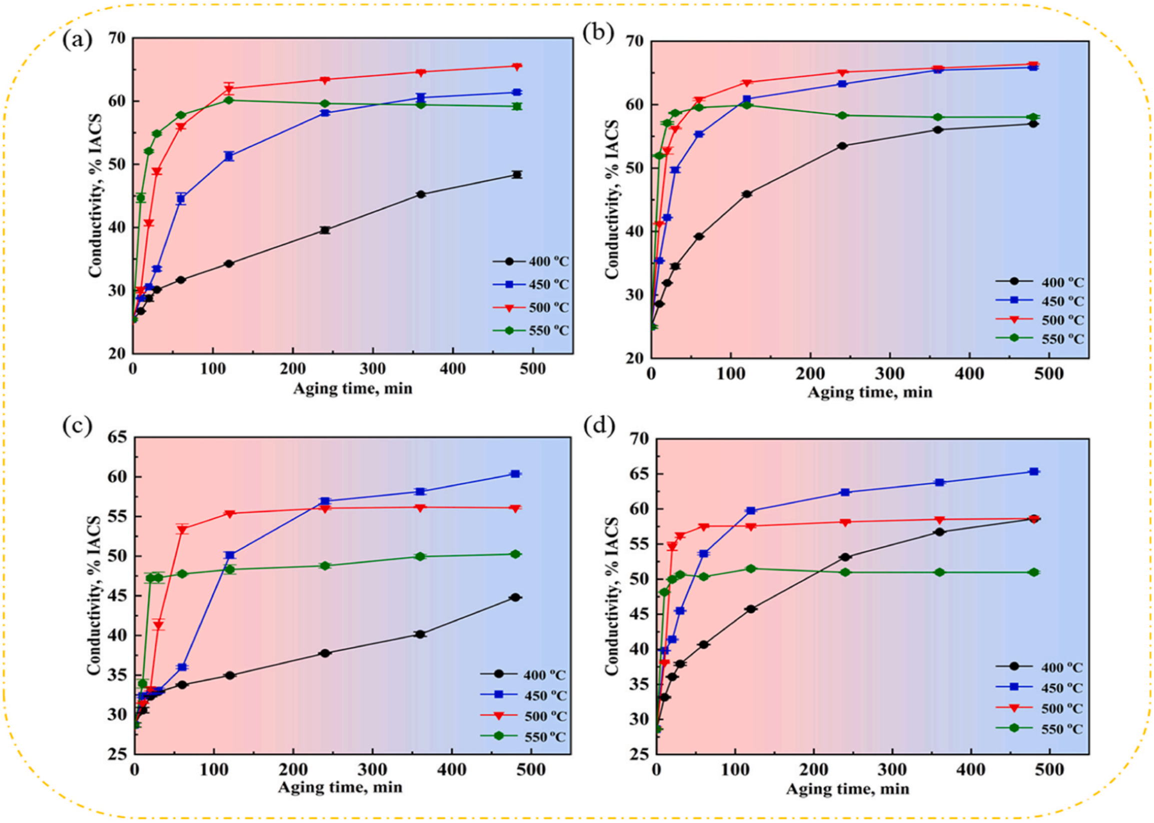

Fig. 8. Electrical conductivity of Cu-Zr-Fe(-Y) alloys after different deformation and aging conditions: (a) Cu-Zr-Fe alloy at 0% cold deformation; (b) Cu-Zr-Fe alloy at 60% cold deformation; (c) Cu-Zr-Fe-Y alloy at 0% cold deformation; (d) Cu-Zr-Fe-Y alloy at 60% cold deformation.

Table 3
The tensile strength of the Cu-Zr-Fe alloys aged at 450 °C.

Cu-Zr-Fe Alloy	Aging time, min		
	60 min	120 min	240 min
Tensile strength, MPa	467.9 (± 4)	512.8 (± 5)	471 (± 4)

Table 4
The tensile strength of the Cu-Zr-Fe-Y alloy aged at 500 °C.

Cu-Zr-Fe-Y Alloy	Aging time, min		
	10 min	20 min	30 min
Tensile strength, MPa	483.8 (± 4)	546.9 (± 3)	525 (± 10)

Table 5
Comparison of tensile strength and conductivity of Cu-Zr-Fe(-Y) alloys with conventional copper alloys.

Alloy	Tensile strength, MPa	Electrical conductivity, %IACS
Cu-Zr-Fe	512.8	60.9
Cu-Zr-Fe-Y	546.9	54.8
Cu-0.3Zr	420	92
Cu-0.3Zr-0.4Cr	450	84
Cu-0.5Zr	482	83
Cu-0.7Cr-0.3Fe	365	74
Cu-1Cr	413	81
Cu-2.3Fe-0.1Sn-0.03 P	450	70
Cu-2.3Fe-0.03 P	401	92

comprehensive properties of the Cu-Zr-Fe alloy. In order to study the distribution of solute atoms in the alloys after aging, EDS observations were made with Y as an example. Fig. 10 shows the surface scan of the Cu-Zr-Fe-Y alloy in the peak aged state. The distribution of each element is more homogeneous compared with the solid solution state. In order to further investigate the microstructure evolution of the alloys during aging, the Cu-Zr-Fe(-Y) alloys subjected to 60% cold deformation aged at 500 °C for 20 min and 240 min were characterized by EBSD. Figs. 11 and 12 show the inverse pole figure (IPF) plots and average grain size distribution of the two Cu-Zr-Fe(-Y) alloys. There are multiple colors in the IPF plots, which are due to the different orientations of the grains within the crystals. The grains are elongated due to cold deformation before aging, and a large number of fine, distortion-free equiaxed grains are produced at the grain boundaries of the deformed grains. The average grain size of the Cu-Zr-Fe alloy aged at 500 °C for 20 min and 240 min is 40 μm and 64.3 μm, respectively, in Fig. 11(c, d). The average grain size of Cu-Zr-Fe-Y alloy aged at 500 °C for 20 min and 240 min is 35.1 μm and 22.3 μm, respectively in Fig. 12(c, d). The addition of Y weakens the grain growth, which originated from Y promoting precipitated phases, which pinned grain boundaries, hindering their migration. It is found by comparing Fig. 11(c, d) with Fig. 12(c, d) that the average grain size of the Cu-Zr-Fe-Y alloy is smaller than the Cu-Zr-Fe alloy, which indicates that Y refines the grain size, and plays the role of fine-grain strengthening. Based on the Hall-Petch formula, the smaller the grain size, the higher the hardness and strength of the alloy, so the addition of Y enhances the hardness and strength of the alloy.

Fig. 13 shows the kernel average misorientation (KAM) diagram of the two Cu-Zr-Fe(-Y) alloys. The geometrically necessary dislocation density [52] of the alloys can be calculated as:

$$\rho^{GND} = \frac{2\theta}{\mu b} \tag{3}$$

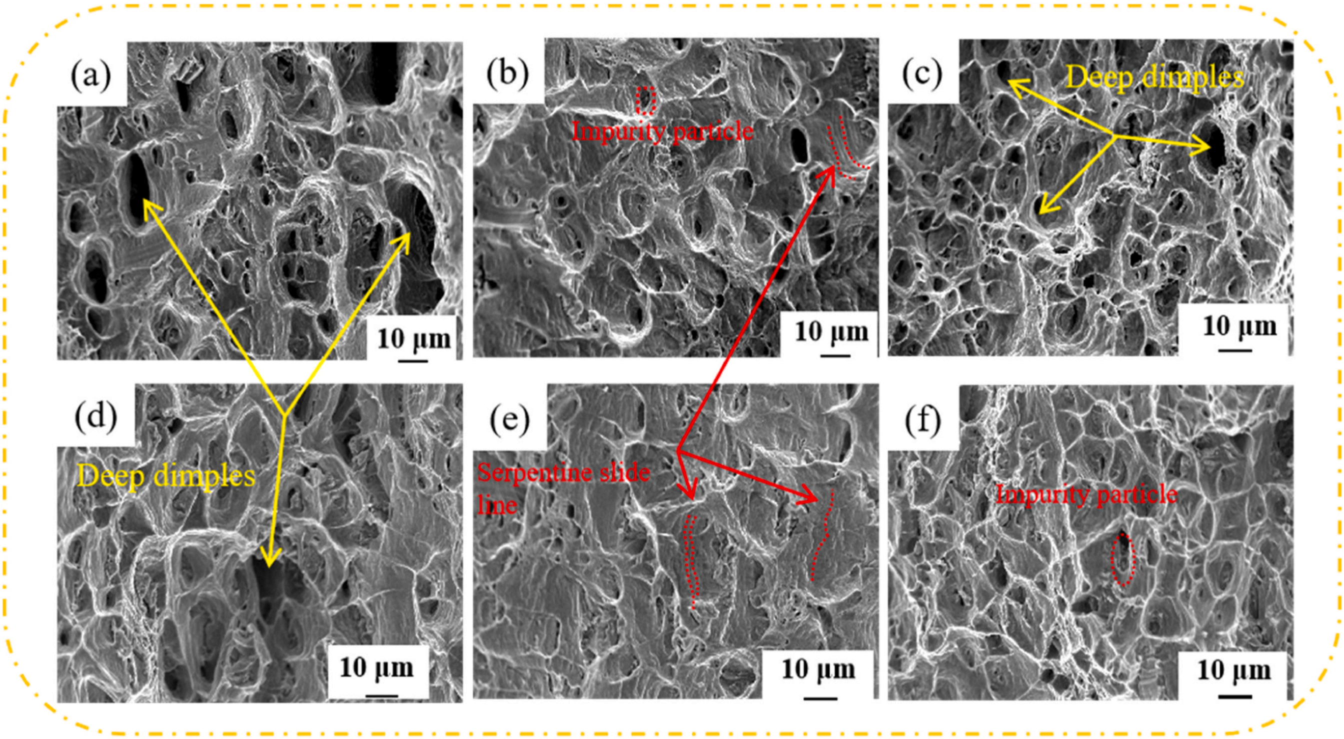

Fig. 9. Tensile fracture morphology of Cu-Zr-Fe(-Y) alloys: (a) Cu-Zr-Fe alloy aged at 450 °C for 60 min; (b) Cu-Zr-Fe alloy aged at 450 °C for 120 min; (c) Cu-Zr-Fe alloy aged at 450 °C for 240 min; (d) Cu-Zr-Fe-Y alloy aged at 500 °C for 10 min; (e) Cu-Zr-Fe-Y alloy aged at 500 °C for 20 min; (f) Cu-Zr-Fe-Y alloy aged at 500 °C for 30 min.

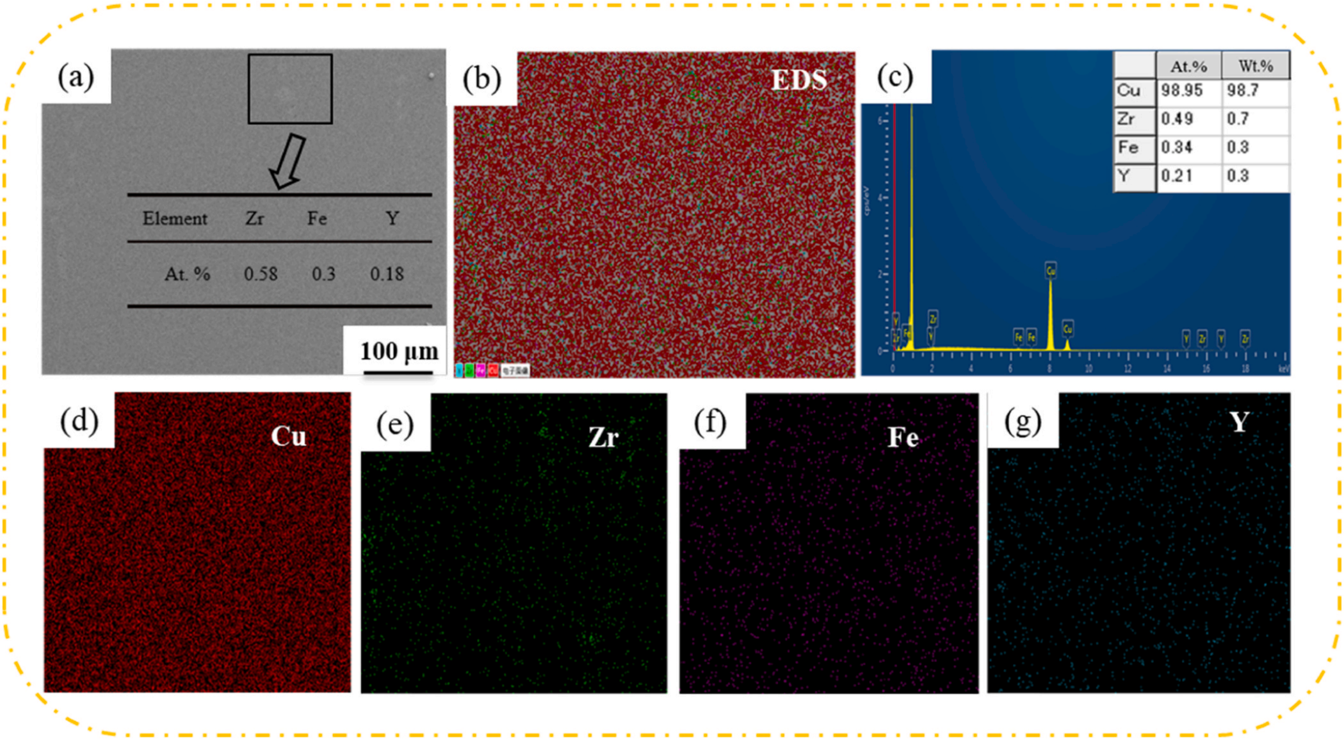

Element	Zr	Fe	Y
At. %	0.58	0.3	0.18

	At.%	Wt.%
Cu	98.95	98.7
Zr	0.49	0.7
Fe	0.34	0.3
Y	0.21	0.3

Fig. 10. SEM morphology and EDS analysis of peak aged Cu-Zr-Fe-Y alloy:(a) SEM image; (b) EDS combined elements image; (c) elemental content; (d) Cu; (e) Zr; (f) Fe; (g) Y maps.

Here, ρ^{GND} is the geometrically necessary dislocation density in m^{-2}, θ denotes the average localized orientation difference in rad, μ is the scanning step size of 2.5 µm, and b is Burger's vector of 0.255 µm.

It is observed from Fig. 13(a, b) that the dislocation density of the Cu-Zr-Fe alloy aged at 500 °C for 20 min and 240 min is 4.49×10^{14} m^{-2} and 4.31×10^{14} m^{-2}, respectively. The dislocation density of the Cu-Zr-

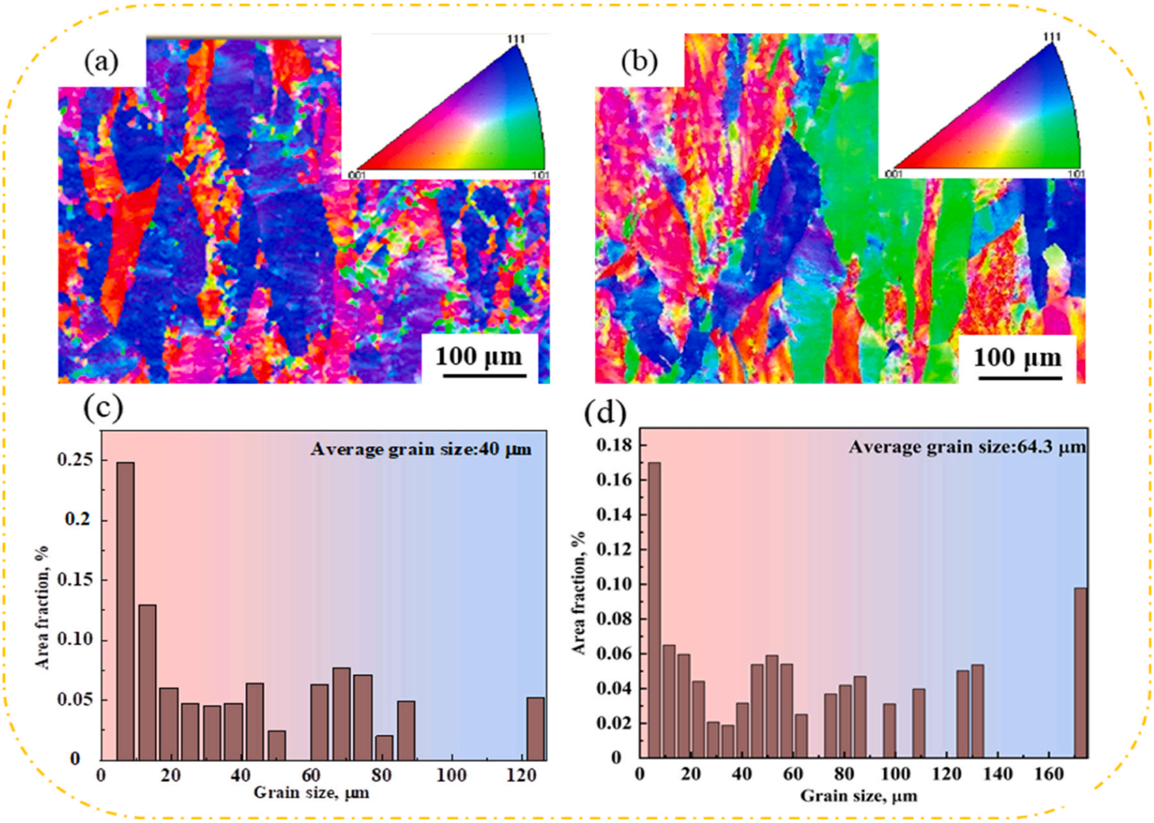

Fig. 11. IPF plots and grain size of Cu-Zr-Fe alloys: (a, c) Cu-Zr-Fe alloy aged at 500 °C for 20 min; (b, d) Cu-Zr-Fe alloy aged at 500 °C for 240 min.

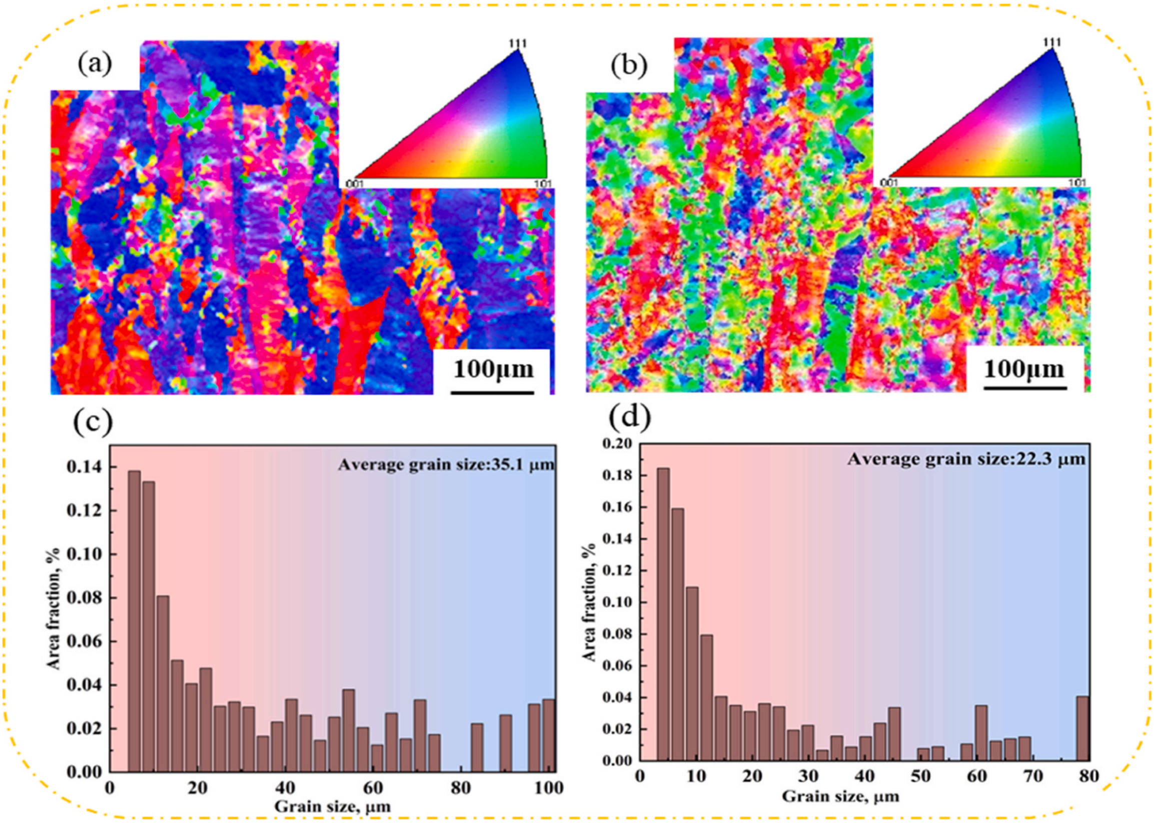

Fig. 12. IPF plots and grain size of Cu-Zr-Fe-Y alloy: (a, c) Cu-Zr-Fe-Y alloy aged at 500 °C for 20 min; (b, d) Cu-Zr-Fe-Y alloy aged at 500 °C for 240 min.

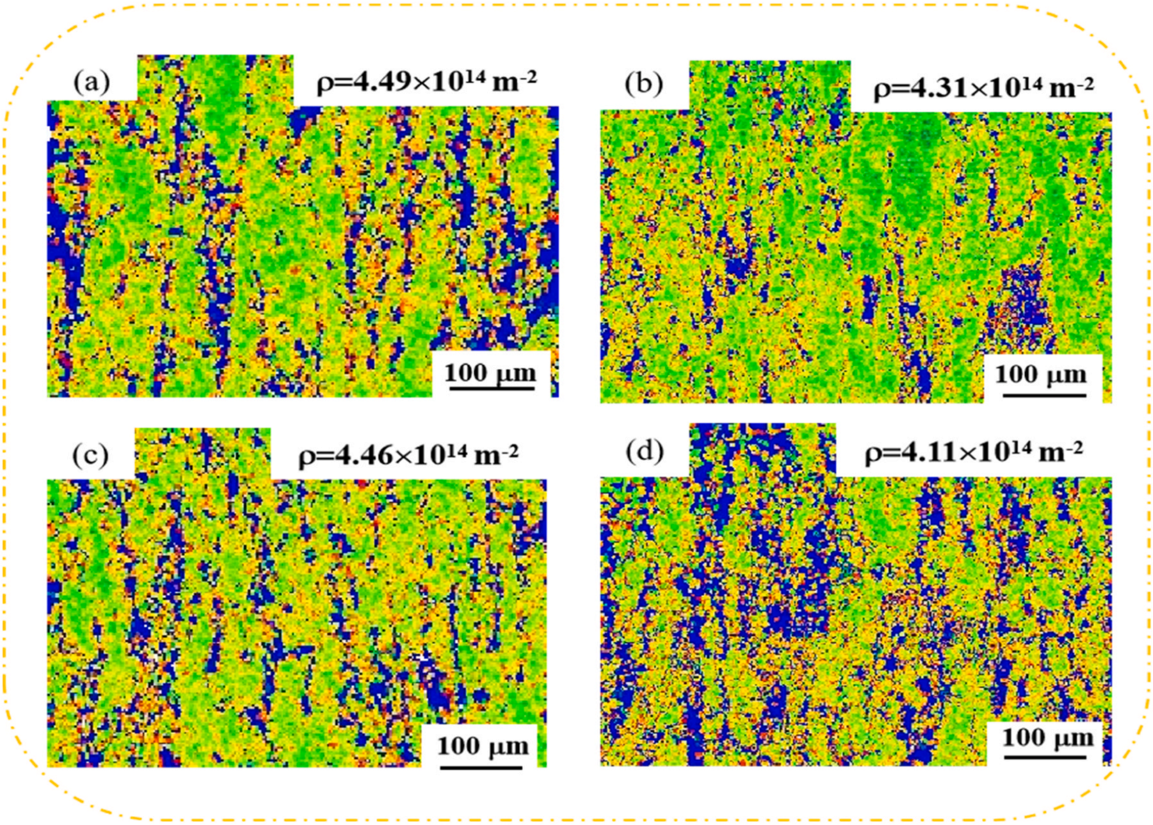

Fig. 13. KAM plots of Cu-Zr-Fe(-Y) alloys: (a) Cu-Zr-Fe alloy aged at 500 °C for 20 min; (b) Cu-Zr-Fe alloy aged at 500 °C for 240 min; (c) Cu-Zr-Fe-Y alloy aged at 500 °C for 20 min; (d) Cu-Zr-Fe-Y alloy aged at 500 °C for 240 min.

Fe-Y alloy aged at 500 °C for 20 min and 240 min is 4.46×10^{14} m^{-2} and 4.11×10^{14} m^{-2}, respectively in Fig. 13(c, d). The decrease in the dislocation density of both alloys with aging time is mainly due to the high energy at the defects in the crystals, recrystallization, and precipitation, which in turn decreases the dislocation density [53]. By comparing Fig. 13(a, c) and Fig. 13(b, d), it is found that the addition of Y decreases the alloy's dislocation density, this suggests that the Y addition accelerates the dislocation depletion and facilitates recrystallization.

Figs. 14 and 15 show the recrystallization distributions of the Cu-Zr-Fe(-Y) alloys under different aging times, respectively. From Fig. 14(c)(d) and 15(c)(d), it can be seen that the recrystallized volume fraction of the Cu-Zr-Fe alloy increases from 5.23% to 6.63% and that of the Cu-Zr-Fe-Y alloy increases from 6.87% to 10.2% with increase of aging time, which indicates that the longer aging time can allow the alloys to recrystallize sufficiently. In addition, by comparing Figs. 14(c) and 15(c) with Figs. 14(d) and 15(d), it can be found that the addition of Y can increase the recrystallization volume fraction, which indicates that Y promotes the recrystallization of the alloy.

Fig. 16 show the orientation angle distribution of Cu-Zr-Fe(-Y) alloys. It can be observed from Fig. 16(a, b), that the Cu-Zr-Fe alloy has 16% of large angle grain boundaries when aged at 500 °C for 20 min, and the percentage of large angle grain boundaries of the alloy aged for 240 min increases to 16.70%. The Cu-Zr-Fe-Y alloy has 16.55% of large angle grain boundaries when aged at 500 °C for 20 min, and the percentage of large angle grain boundaries of the alloy aged for 240 min is elevated to 25.10%, as seen in Fig. 16(c, d). It is known that the size and the orientation angle of the grains on both sides of the grain boundary are closely related to recrystallization. The larger the orientation angle, the higher the migration rate of the grain boundaries, more conducive to the generation of fine recrystallized grains strengthening the matrix [54, 55]. A comparison of the two alloys reveals that the Cu-Zr-Fe-Y alloy has a higher percentage of large-angle grain boundaries, which indicates that the Y addition allows the alloy to fully recrystallize, consistent with the previous analysis results.

In order to investigate the texture evolution of Cu-Zr-Fe(-Y) alloys after different aging conditions, pole figure, inverse pole figures, and the corresponding distribution of crystal texture were obtained in Figs. 17 and 18. The texture of Cu-Zr-Fe alloys aged at 500 °C for 20 min and 240 min is {011}< 100 > Goss texture and {001}< 100 > Cube texture, and the main texture of Cu-Zr-Fe-Y alloys aged at 500 °C for 20 min and 240 min is {011}< 100 > Goss texture and {112}< 111 > Copper texture, and the maximum texture strength of Cu-Zr-Fe-Y alloys was greater than that of Cu-Zr-Fe alloys. Furthermore，it can be seen from Figs. 17(c, d) and 18(c, d) that the addition of Y caused a change in the distribution of grain surface texture strength. The comprehensive analysis shows that Y can change the type, distribution and strength of alloy texture.

Fig. 19 shows the texture and contents of the alloys, which are analyzed as an example of Cu-Zr-Fe-Y alloy. Fig. 19(a, b) show the texture composition of Cu-Zr-Fe-Y alloy aged at 500 °C for 20 min and 240 min, and the corresponding contents are shown in Fig. 19(d). After 20 min aging, the percentage of Cube, Goss, Brass, Copper, and S texture is 2.9%, 8.47%, 22.9%, 17.9%, and 28.1%, respectively. When the aging time was increased to 240 min, the percentage of Cube, Goss, Brass, Copper, and S texture was 7.14%, 3.4%, 2.67%, 23.2%, and 28.4%, respectively. It is a known fact that the properties of the alloys are closely related to the content of these five main textures, and the stronger the texture, the better the performance [56]. Therefore, the overall performance of the alloys aged for 20 min is superior to 240 min aging. In addition, Fig. 19(c) shows the texture content of Cu-Zr-Fe alloy under this aging condition, it is observed comparing Fig. 19(c) and Fig. 19(d) that the Y addition has led to an overall increase in the content of the five main textures, which also proves that the performance of the

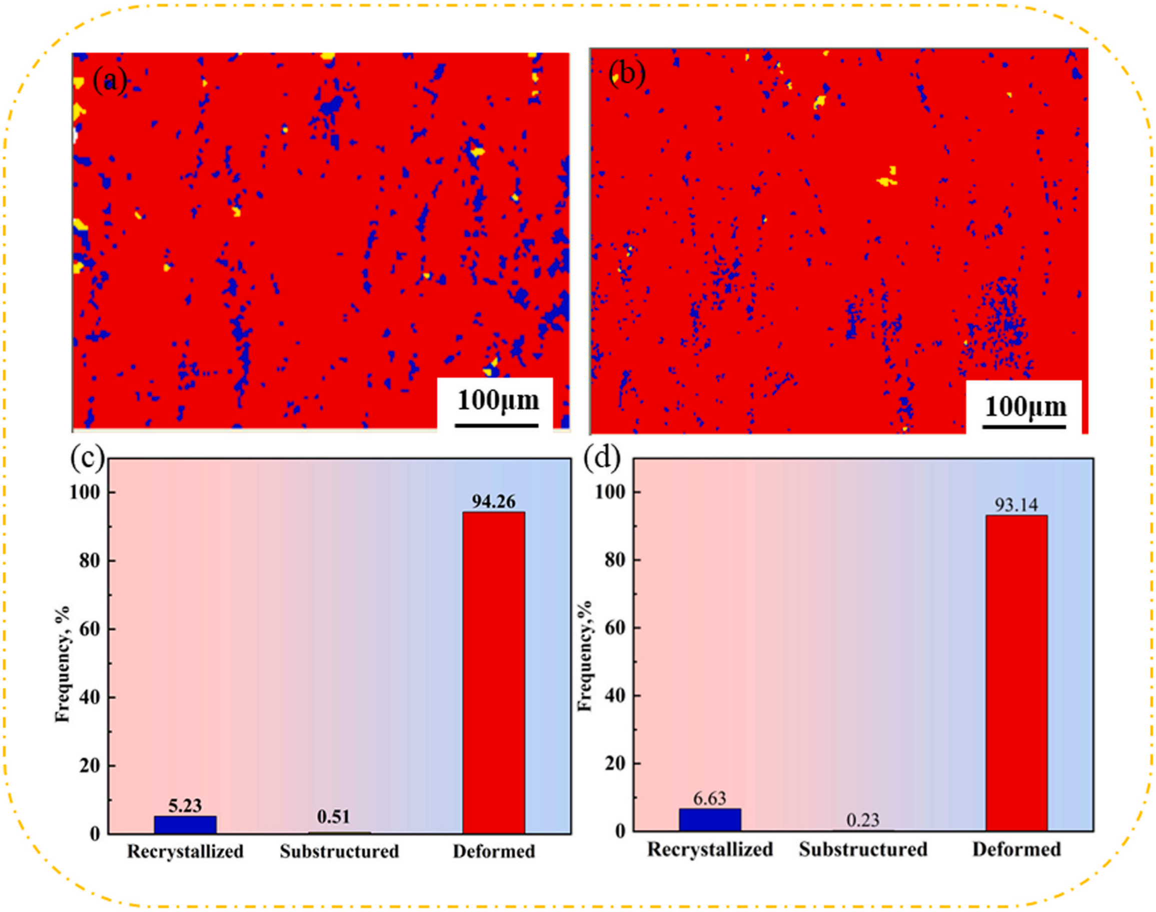

Fig. 14. Recrystallization distribution of Cu-Zr-Fe alloy at aging temperature of 500 °C (a, c) Cu-Zr-Fe alloy aged at 500 °C for 20 min; (b, d) Cu-Zr-Fe alloy aged at 500 °C for 240 min;.

Cu-Zr-Fe-Y alloy is superior to the Cu-Zr-Fe alloy.

3.4. TEM analysis

In order to investigate the types of precipitated phases during the aging process, the precipitated phases of Cu-Zr-Fe-Y alloy after 60% cold deformation and 500 °C aging for 20 min are discussed. Fig. 20 shows the TEM organization of Cu-Zr-Fe-Y alloy under this experimental condition. It can be observed from Fig. 20(a) that there are a large number of fine precipitated phases diffusely distributed in the matrix, which play the role of diffusion strengthening. In addition, typical microstructure such as dislocation tangles, dislocation cell walls and dislocation cells in alloys can be clearly found in Figs. 20(b) and 20(c). The formation of this microstructure is due to the pinning effect of the precipitated phases and the interaction between the precipitated phases and dislocations as obstacles to dislocation motion, which in turn improves the hardness and strength of the alloy and strengthens the matrix. Meanwhile, the phenomenon of dislocation bypassing appears, pointed by the red arrow in Fig. 20(b), where the dislocation motion encounters the diffusely distributed particles by passing them to continue the motion and leaving the dislocation ring as the Orowan strengthening mechanism. Besides, the appearance of twinned crystals is observed in Fig. 20(d), which is a special kind of eutectic grain boundary that hinders the formation of substructures and delays the occurrence of dynamic recrystallization [57]. Fig. 20(e) shows the SAED model of Fig. 20(a), where one set of bright diffraction spots and two sets of weak diffraction spots are observed. The bright spots are the diffraction spots of the Cu substrate, the set of weak spots indicated by the yellow arrows are the diffraction spots of the Cu_5Zr precipitated phase, and the set of weak spots indicated by the red arrows are the additional diffraction spots caused by secondary diffraction. Furthermore, the presence of many parallel streaks can be observed in Fig. 20(f), which are due to double diffraction between the matrix and precipitation phases [14].

In order to investigate the composition of the precipitated phase, the high-resolution morphology of the alloy shown in Fig. 21(a) was obtained, and the Fourier variations and inverse Fourier transform images of the region A in Fig. (a) are shown in Fig. 21(b, c), and the Fourier variations and inverse Fourier transform images of the region B in Fig. (a) are shown in Fig. 21(d, e). The precipitated phase was determined to be γ-Fe phase by standard diffraction spot pattern calibration, and it was found from Figs. (b, d) that the spots of the precipitated phase and the substrate were almost coincident. However, from the inverse Fourier transform of the precipitated phase in Fig. (c), the presence of dislocations and periodic stress field is found, and also because the lattice constants of the γ-Fe phase and the Cu substrate are very close to each other. Therefore, to further determine the consistency between them, the degree of mismatch between the two phases can be calculated according to Eq. (4).

$$\delta = \frac{d_1 - d_2}{d_1} \tag{4}$$

Where δ is the mismatch between the precipitated phase and the matrix, d_1 is the matrix lattice constant ($d_1 = 0.2490$ nm), d_2 is the precipitated phase lattice constant ($d_2 = 0.2467$ nm), it can be seen from the calculation that the mismatch between $(0\ 2\ \overline{2})_{\gamma\text{-Fe}}$ and $(0\ \overline{2}\ 2)_{Cu}$ is 0.9%, it shows that the γ-Fe phase is in complete coherent with the Cu matrix. The presence of the precipitated phase pins dislocations and hinders the slipping and climbing of dislocations, which can effectively strengthen

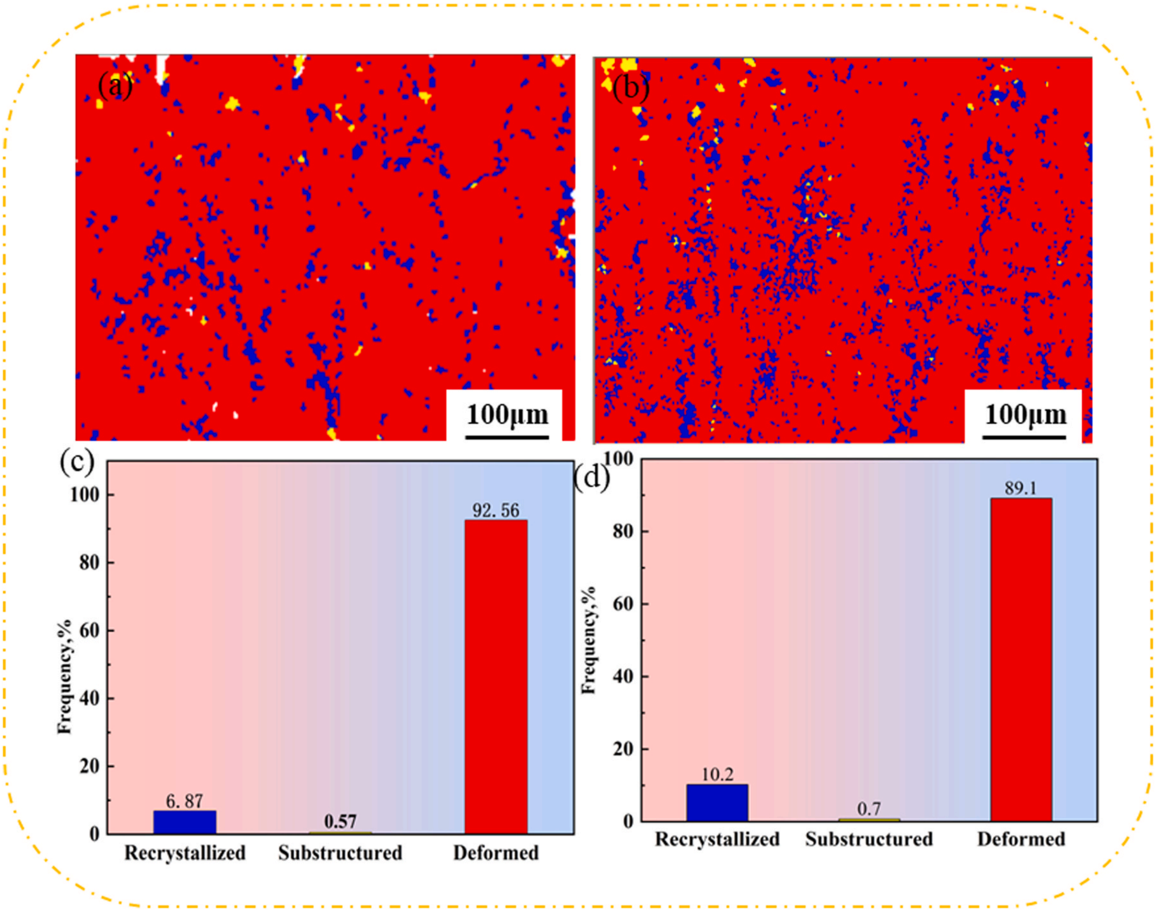

Fig. 15. Recrystallization distribution of Cu-Zr-Fe-Y alloy at aging temperature of 500 °C. (a, c) Cu-Zr-Fe-Y alloy aged at 500 °C for 20 min; (b, d) Cu-Zr-Fe-Y alloy aged at 500 °C for 240 min;.

the matrix, and the precipitated phase attenuates the electron scattering effect on the substrate, which helps to improve the electrical conductivity of the alloy.

Fig. 22 shows the TEM organization of Cu-Zr-Fe-Y alloy after 60% cold deformation and aging at 500 °C for 120 min Fig. 22(a) shows the high-resolution morphology of the alloy under this aging condition, from which the presence of long strip-like precipitated phases can be clearly observed. Fig. 22(b)(c) shows the Fourier transform and inverse Fourier transform images of Fig. 22(a), respectively, and the phase was determined to be the α-Fe phase by diffraction pattern calibration, and from Fig. 22(c), the crystalline spacing of $(\bar{1}\,\bar{1}\,1)_{Cu}$ is 0.214 nm, and the crystalline spacing of$(0\,\bar{1}\,1)_{\alpha\text{-Fe}}$ is 0.203 nm, and the mismatch degree of 5.1% can be calculated from Eq. 4, indicating that with the prolongation of aging time with the matrix, there exists a part of the γ-Fe phase, which is complete coherent with the matrix, transformed into the semi-coherent α-Fe phase, which explains the decrease in microhardness of the Cu-Zr-Fe-Y alloy in the over-aging stage.

3.5. Strengthening mechanisms

Copper alloys have four main strengthening mechanisms: solid solution, deformation, fine grain and precipitation strengthening, which are analyzed in detail by taking the peak-aged Cu-Zr-Fe-Y alloy as an example. The yield strength of Cu-Zr-Fe-Y alloy can be expressed by Eq.5:

$$\sigma = \sigma_0 + \sigma_{ss} + \sigma_{ds} + \sigma_p + \sigma_{GB} \tag{5}$$

Here, σ_0 is the yield strength of copper matrix ($\sigma_0 = 20$ MPa)[58], σ_{ss} represents solid solution strengthening contribution, σ_{ds}represents deformation strengthening contribution, σ_{GB} represents fine grain strengthening contribution and σ_p represents precipitation strengthening contribution.

The solid solution strengthening contribution of the Cu-Zr-Fe-Y alloy can be described as:

$$\sigma_{ss} = G\left(|\delta| + \frac{1}{20}\right)|\eta|^{\frac{3}{2}}\sqrt{\frac{x_a}{3}} \tag{6}$$

Here, G is the shear modulus of the copper alloy (G=46 GPa), δ is the lattice change factor (δ = 0.1105), η is the change factor of the shear modulus of the alloy before and after the solid solution treatment (η = 0.3171), and x_a is the mass fraction of solute atoms. The Zr, Fe, and Y contents of the Cu-Zr-Fe-Y alloy are 0.58%, 0.3%, and 0.18%, respectively, as shown in Fig. 10(a). Therefore, the solid solution strengthening contribution of Cu-Zr-Fe-Y alloy can be calculated as 78.1 MPa.

The solid solution Cu-Zr-Fe-Y alloy was subjected to 60% cold deformation, which produced a large number of dislocations, twins, and other organizational strengthening of the matrix during the cold deformation process. The contribution produced by deformation strengthening is:

$$\sigma_{ds} = M\alpha Gb\sqrt{\rho} \tag{7}$$

Here, M is the Taylor coefficient of the alloy M= 3.06, α is the geometrical constant α = 0.3, G is the shear modulus of the copper alloy (G=46 GPa), b is the Burger's vector b= 0.2556 nm, and ρ is the dislocation density of the alloy in Fig. 13(c). Therefore, the contribution resulting from deformation strengthening was calculated to be 221.46 MPa.

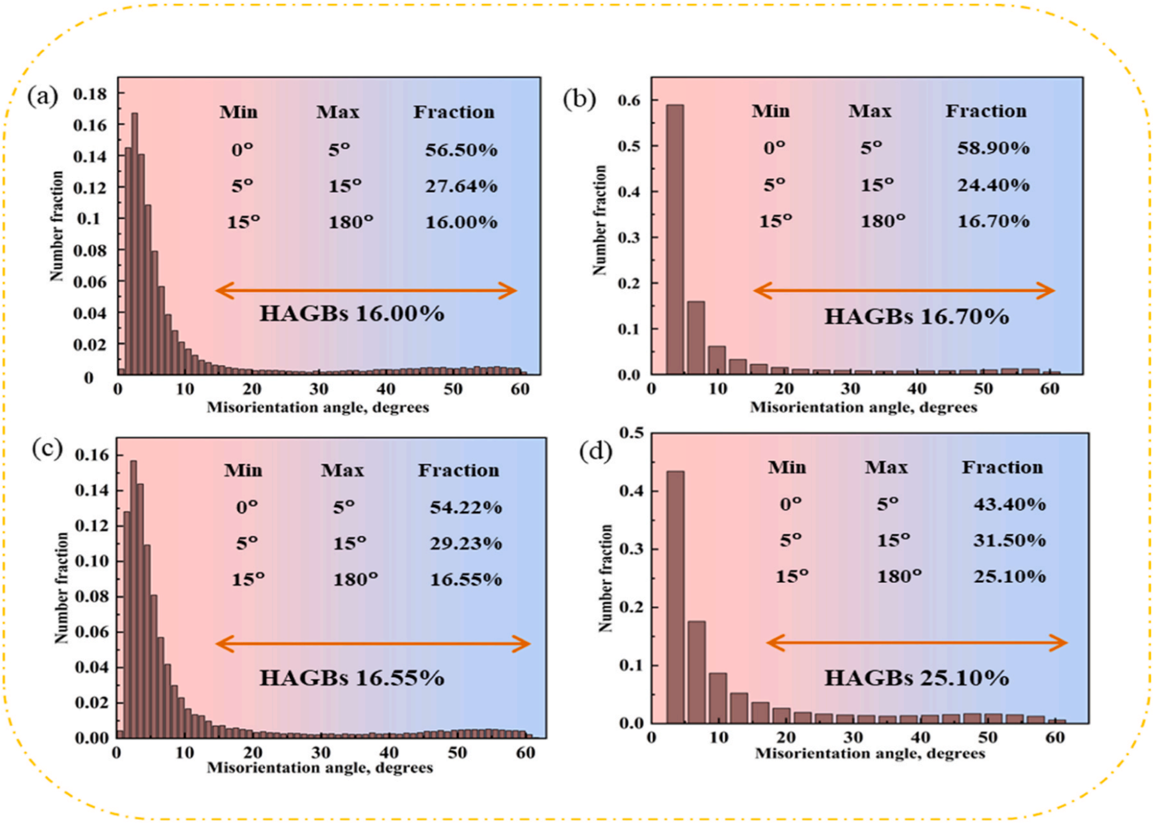

Fig. 16. Orientation angle distribution of Cu-Zr-Fe-(Y) alloys: (a) Cu-Zr-Fe alloy aged at 500 °C for 20 min; (b) Cu-Zr-Fe alloy aged at 500 °C for 240 min; (c) Cu-Zr-Fe-Y alloy aged at 500 °C for 20 min; (d) Cu-Zr-Fe-Y alloy aged at 500 °C for 240 min.

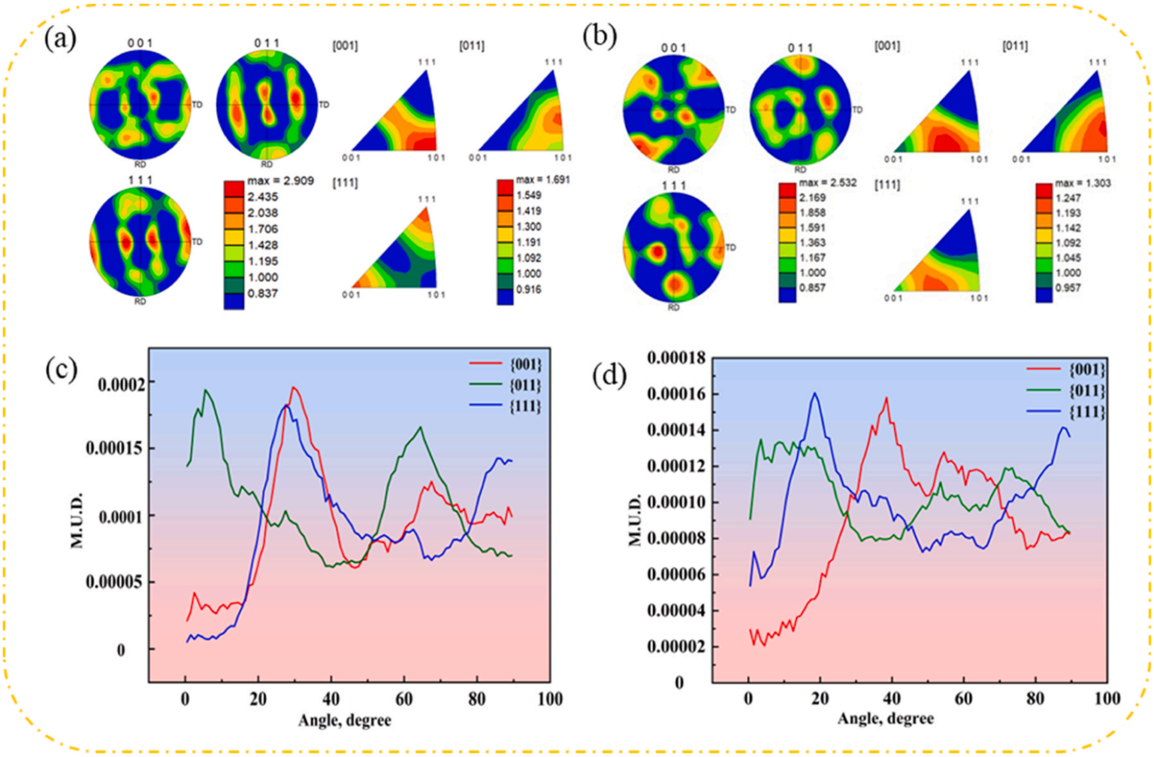

Fig. 17. Pole figures, inverse pole figures, and texture distribution of Cu-Zr-Fe alloys aged at 500 °C for: (a, c) 20 min; (b, d) 240 min.

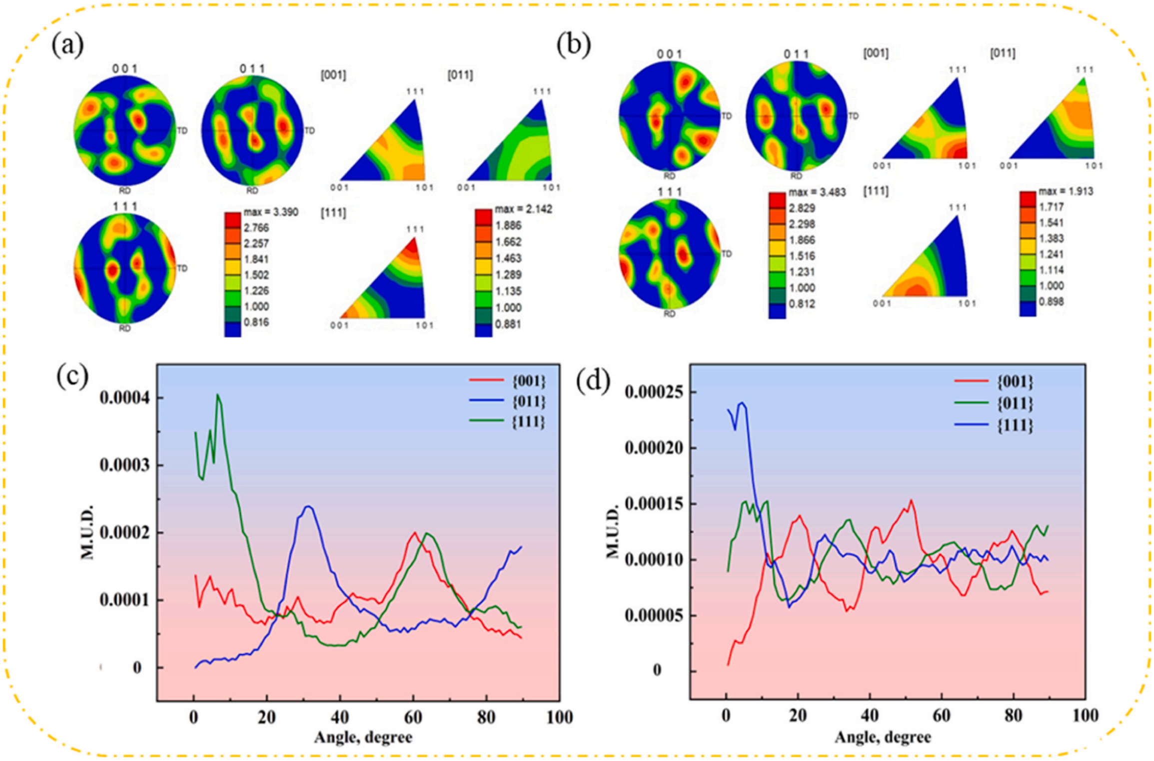

Fig. 18. Pole figures, inverse pole figures, and texture distribution of Cu-Zr-Fe-Y alloy aged at 500 °C for: (a, c) 20 min; (b, d) 240 min.

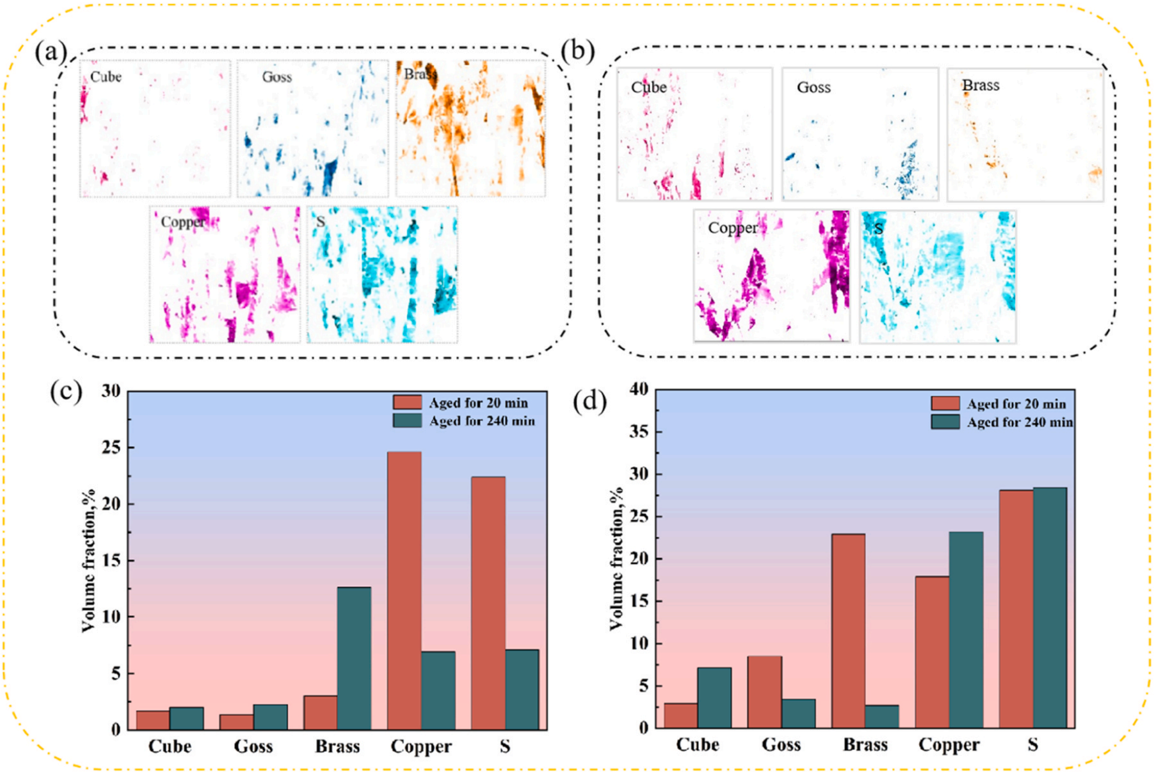

Fig. 19. Texture composition and percentages of Cu-Zr-Fe(-Y) alloys: (a) Cu-Zr-Fe-Y alloy aged at 500 °C for 20 min; (b) Cu-Zr-Fe-Y alloy aged at 500 °C for 240 min; (c) Cu-Zr-Fe alloy aged at 500 °C for 20 min and 240 min; (d) Cu-Zr-Fe-Y alloy aged at 500 °C for 20 min and 240 min.

The contribution of fine grain strengthening can be expressed by the Hall-Petch equation:

$$\sigma_{GB} = \frac{K_y}{\sqrt{d}} \tag{8}$$

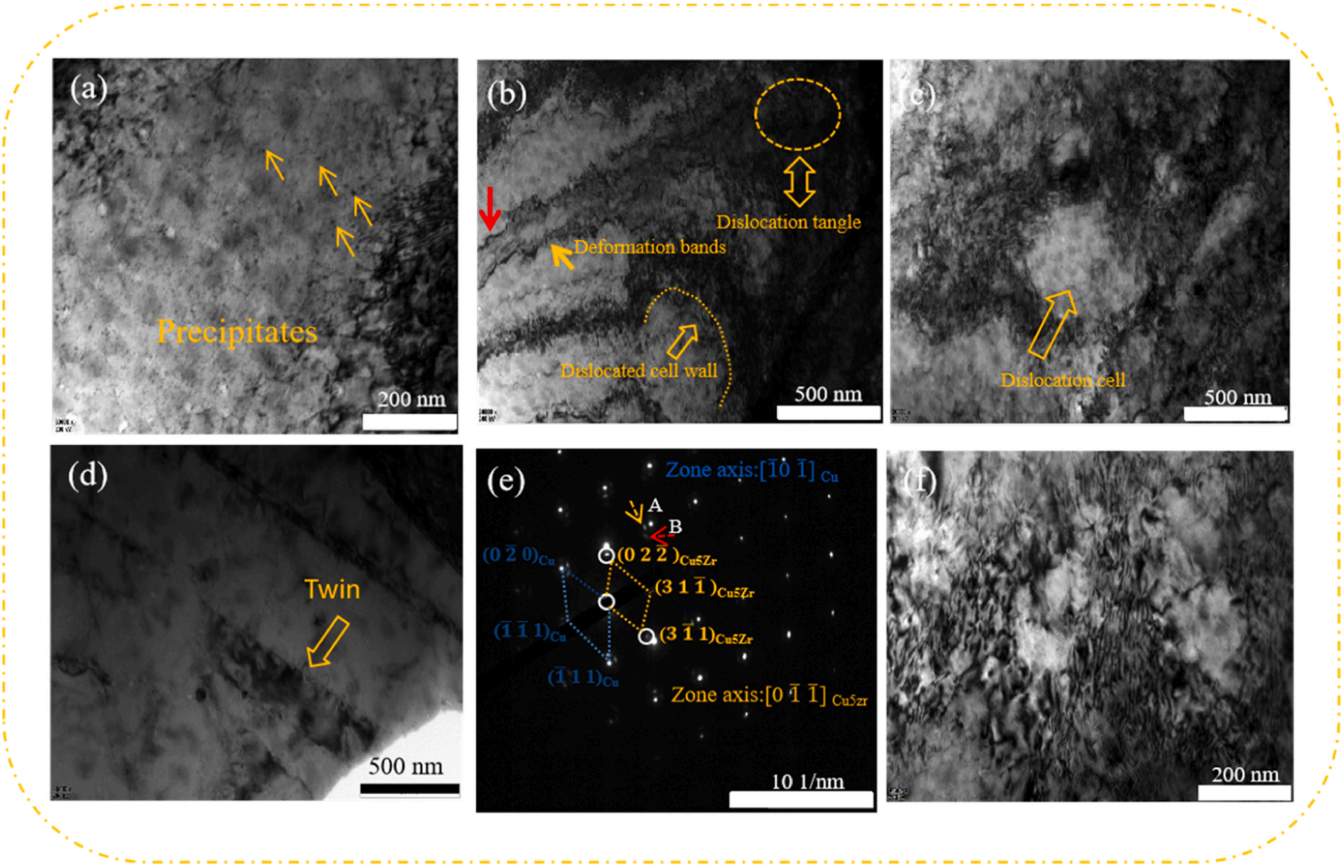

Fig. 20. TEM microstructure of Cu-Zr-Fe-Y alloy aged at 500 °C for 20 min; (a) (b) and (c) bright field images; (d) twin texture; (e) FFT pattern of Fig. (a); (f) bright field images.

Here, K_y is the Hall-Petch coefficient (K_y=150 MPa μm$^{\frac{1}{2}}$), d is the average grain size in Fig. 11(c). Thus, the contribution of the alloy fine grain strengthening is 25.3 MPa.

The precipitation of precipitated phases and the interaction between precipitated phases and dislocations during aging of alloys play a very important role in enhancing the strength of alloys, and this precipitation strengthening mechanism can be expressed by the Orowan-Ashby equation [59]:

$$\sigma_p = 0.81 \times \frac{MGb}{2\pi(1-\upsilon)^{1/2}} \times \frac{\ln(\frac{d_p}{b})}{(\lambda - d_p)} \tag{9}$$

Here, G is the shear module of copper alloy (G=46 GPa), M is the Taylor factor for the fcc matrix (M=3.06), ν is the Poisson's ratio ($\nu = 0.34$), b is the Burgers vector of copper alloy (b=0.2556 nm), $d_p$is the average size of precipitates, λ is the spacing between particles in the glide plane, which can be expressed as Eq. 10:

$$\lambda = \frac{1}{2} d_p \sqrt{\frac{3\pi}{2f_p}} \tag{10}$$

Here, f_p is the volume fraction of precipitates, $d_p$and $f_p$can be calculated by zooming in on the TEM brightfield image ($d_p = 7.1$ nm, $f_p = 0.76\%$). Therefore, the degree of precipitation strengthening of the alloy can be calculated as σ_p= 233.6 MPa. Finally, the yield strength of Cu-Zr-Fe-Y alloy can be calculated to be about:$\sigma = \sigma_0 + \sigma_{ss} + \sigma_{ds} + \sigma_{GB} + \sigma_p$= 20 + 78.1 + 221.5 + 25.3 + 233.6 = 578.5 MPa, the theoretical values are slightly higher than measured values (546.9 MPa), this is due to the large size of particles such as α-Fe. It is seen through the above analysis that the main strengthening mechanism of the Cu-Zr-Fe-Y alloy during aging is precipitation strengthening and deformation strengthening.

4. Conclusions

1) Two Cu-Zr-Fe(-Y) alloys were solid solution treated at 930 °C for 60 min, resulting in a number of black dot-like eutectic particles, accompanied by a large number of generated annealing twins.
2) Under 60% cold rolling, The optimal aging process parameters for the two alloys were 450 °C aging for 120 min and 500 °C aging for 20 min, with the microhardness, electrical conductivity, and tensile strength of 60.9% IACS, 162.4 HV, 512.8 MPa, 54.8% IACS, 177.7 HV, and 546.9 MPa, respectively. The rare earth Y element improves the microhardness and strength of the alloy with a slight decrease in electrical conductivity, which significantly optimizes the performance of the alloy.
3) EBSD analysis of the two alloys after 60% cold deformation and 500 °C aging for 20 min and 240 min revealed that the Y addition refines the grains, reduces the dislocation density, enhances the texture strength, and facilitates the onset of recrystallization of the alloys.
4) The age-hardening effect of Cu_5Zr and γ-Fe precipitation phases pinning dislocations is the main reason for the strengthening of the alloy. The precipitation strengthening and deformation strengthening are the main strengthening mechanisms.

CRediT authorship contribution statement

Li Xu: Investigation. **Volinsky Alex A.:** Writing – review & editing. **Tian Caijiao:** Supervision. **Tian Baohong:** Resources, Supervision. **Guo Mi Xue:** Conceptualization, Formal analysis, Methodology, Writing – original draft. **Zhou Meng:** Project administration, Resources. **Zou Jin:**

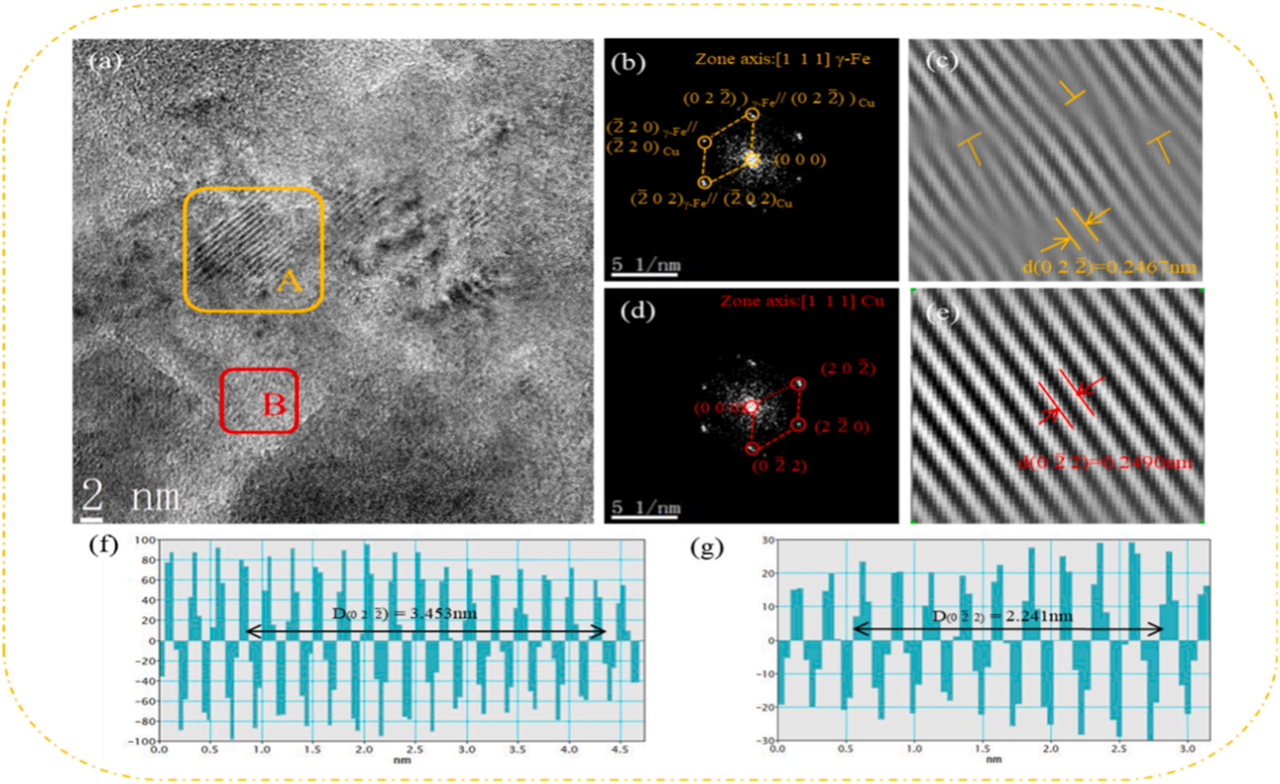

Fig. 21. TEM microstructure of Cu-Zr-Fe-Y alloy aged at 500 °C for 20 min; (a) HRTEM image of the Cu-Zr-Fe-Y alloy taken from Fig. 18(f); (b)FFT pattern of the A framed region in (a); (c) IFFT pattern of image of (b) masking $(0\ 2\ \bar{2})_{\gamma\text{-Fe}}$ and $(0\ 2\bar{2})_{Cu}$ spots; (d)FFT pattern of the B framed region in (a); (e) IFFT pattern of image of (d) masking $(0\ 2\ \bar{2})_{Cu}$ and $(0\ \bar{2}\ 2)_{Cu}$ spots; (f) grain spacing of $(0\ 2\ \ \bar{2})_{\gamma\text{-Fe}}$; (g) grain spacing of $(0\ \bar{2}\ 2)_{Cu}$.

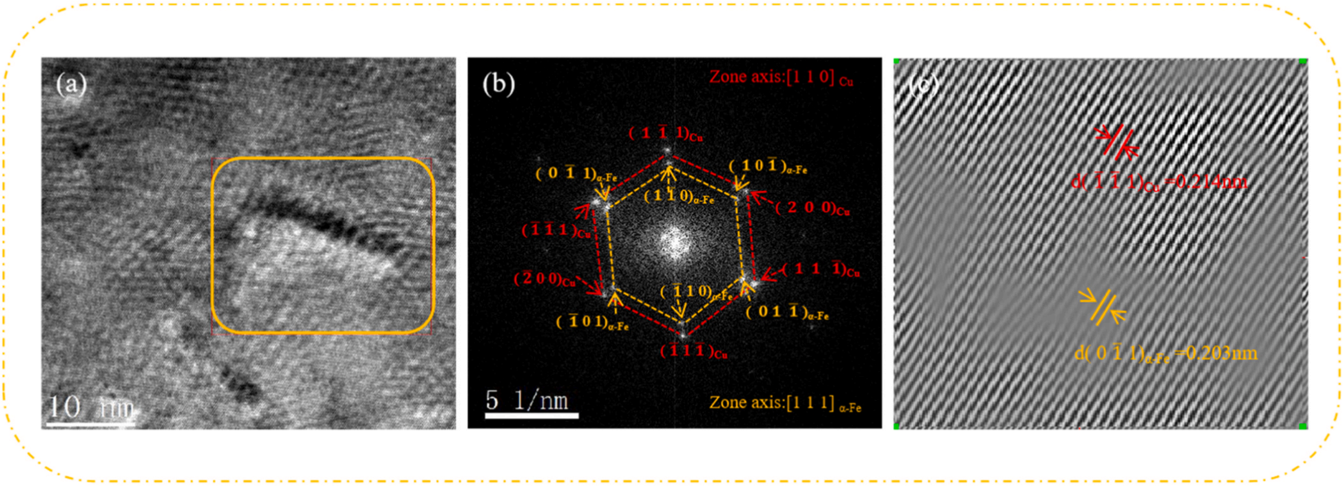

Fig. 22. TEM microstructure of Cu-Zr-Fe-Y alloy aged at 500 °C for 120 min; (a) HRTEM image; (b) FFT pattern of the yellow framed region in Fig. (a); (c) IFFT pattern of the yellow framed region in Fig. (a).

Resources, Supervision. **ZHANG YI:** Funding acquisition, Writing – review & editing. **Bai Qian:** Supervision. **Jing Ke:** Resources, Supervision. **Hu Haoyan:** Formal analysis.

Declaration of Competing Interest

The authors declare that they have no known competing financial interests or personal relationships that could have appeared to influence the work reported in this paper.

Data Availability

The data that has been used is confidential.

Acknowledgements

This research was supported by the National Natural Science Foundation of China (52071134), the Natural Science Foundation of Henan Province (232300420089), the Technology Innovation Center of Graphene Metrology and Standardization for State Market Regulation

(AKYKF2309), the Program for Innovative Research Team at the University of the Henan Province (22IRTSTHN001), the China Postdoctoral Science Foundation (2023TQ0107), Key Research and Development Program of Jiangxi Province (20224BBE52002).

References

[1] K.M. Liu, Z.Y. Jiang, H.T. Zhou, D.P. Lu, A.D. Atrens, Y.L. Yang, Effect of heat treatment on the microstructure and properties of deformation-processed Cu-7Cr in situ composites, J. Mater. Eng. Perform. 24 (11) (2015) 4340–4345, https://doi.org/10.1007/s11665-015-1747-z.

[2] Q. Lei, Z. Li, Y. Gao, X. Peng, B.J.M. Derby, Microstructure and mechanical properties of a high strength Cu-Ni-Si alloy treated by combined aging process. J. Alloy. Compd. 695 (2017) 2413–2423, https://doi.org/10.1016/j.jallcom.2016.11.137.

[3] X.L. Guo, Z. Xiao, W.T. Qiu, Z. Li, Z.Q. Zhao, X. Wang, Y.B. Jiang, Microstructure and properties of Cu-Cr-Nb alloy with high strength, high electrical conductivity and good softening resistance performance at elevated temperature, Mater. Sci. Eng., A. Struct. Mater.: Prop., Misrostruct. Process. 749 (2019) 281–290, https://doi.org/10.1016/j.msea.2019.02.036.

[4] Z. Zhao, Y. Zhang, B.H. Tian, Y.L. Jia, Y. Liu, K.X. Song, A.A. Volinsky, Co effects on Cu-Ni-Si alloys microstructure and physical properties, J. Alloy. Compd.: Interdiscip. J. Mater. Sci. Solid-State Chem. Phys. 797 (2019) 1327–1337, https://doi.org/10.1016/j.jallcom.2019.05.135.

[5] Y. Zhang, H.L. Sun, A.A. Volinsky, B.H. Tian, K.X. Song, B.J. Wang, Y. Liu, Hot workability and constitutive model of the Cu-Zr-Nd alloy, Vacuum 146 (2017) 35–43, https://doi.org/10.1016/j.vacuum.2017.09.017.

[6] M. Azimi, G.H. Akbari, Development of nano-structure Cu–Zr alloys by the mechanical alloying process, J. Alloy. Compd. 509 (1) (2011) 27–32, https://doi.org/10.1016/j.jallcom.2010.08.071.

[7] J.P. Tu, W.X. Qi, Y.Z. Yang, F. Liu, J.T. Zhang, G.Y. Gan, N.Y. Wang, X.B. Zhang, M. S. Liu, Effect of aging treatment on the electrical sliding wear behavior of Cu-Cr-Zr alloy, Wear 249 (10-11) (2002) 1021–1027, https://doi.org/10.1016/s0043-1648(01)00843-2.

[8] A. Bodyakova, R. Mishnev, A. Belyakov, R. Kaibyshev, Effect of chromium content on precipitation in Cu–Cr–Zr alloys, J. Mater. Sci. 57 (27) (2022) 13043–13059, https://doi.org/10.1007/s10853-022-07454-8.

[9] F.X. Huang, J.S. Ma, H.L. Ning, Z.T. Geng, C. Lu, S.M. Guo, X.T. Yu, T. Wang, H. Li, H.F. Lou, Analysis of phases in a Cu–Cr–Zr alloy, Scr. Mater. 48 (1) (2003) 97–102, https://doi.org/10.1016/s1359-6462(02)00353-6.

[10] Y. Zhang, A.A. Volinsky, H.T. Tran, Z. Chai, P. Liu, B.H. Tian, Y. Liu, Aging behavior and precipitates analysis of the Cu–Cr–Zr–Ce alloy, Mater. Sci. Eng.: A 650 (2016) 248–253, https://doi.org/10.1016/j.msea.2015.10.046.

[11] K. Wang, K.F. Liu, J.B. Zhang, Microstructure and properties of aging Cu–Cr–Zr alloy, Rare Met. 33 (2014) 134–138, https://doi.org/10.1007/s12598-014-0244-0.

[12] S.C. Krishna, N.K. Gangwar, A.K. Jha, B. Pant, K.M. George, Enhanced strength in Cu-Ag-Zr alloy by combination of cold working and aging, J. Mater. Eng. Perform. 23 (2014) 1458–1464, https://doi.org/10.1007/s11665-014-0882-2.

[13] S.L. Fu, P. Liu, X.H. Chen, H.L. Zhou, F.C. Ma, W. Li, K. Zhang, Effect of aging process on the microstructure and properties of Cu–Cr–Ti alloy, Mater. Sci. Eng.: A 802 (2021) 140598, https://doi.org/10.1016/j.msea.2020.140598.

[14] H.T. Zhou, J.W. Zhong, X. Zhou, Z.K. Zhao, Q.B. Li, Microstructure and properties of Cu–1.0Cr–0.2Zr–0.03Fe alloy, Mater. Sci. Eng.: A 498 (1-2) (2008) 225–230, https://doi.org/10.1016/j.msea.2008.07.061.

[15] H.Y. Yang, T. Lv, Y.Q. Bu, J.M. Wu, Y.T. Fang, J.B. Liu, H.G. Wang, CALPHAD-based design and preparation of high-strength, high-conductivity Cu–Fe–Zr alloys, J. Mater. Sci. (2023), https://doi.org/10.1007/s10853-022-08087-7.

[16] F.A. Guo, C.J. Xiang, C.X. Yang, X.M. Cao, S.G. Mu, Y.Q. Tang, Study of rare earth elements on the physical and mechanical properties of a Cu–Fe–P–Cr alloy, Mater. Sci. Eng.: B 147 (1) (2008) 1–6, https://doi.org/10.1016/j.mseb.2007.10.011.

[17] X. Jiang, S.H. Song, Enhanced hot ductility of a Cr-Mo low alloy steel by rare earth cerium. Mater. Sci. Eng., A. Struct. Mater.: Prop., Microstruct. Process. 613 (2014) 171–177, https://doi.org/10.1016/j.msea.2014.06.094.

[18] T.M. Wang, M.Y. Li, H.J. Kang, W. Wang, C.L. Zou, Z.N. Chen, Effects of trace La additions on the microstructures and properties of nanoprecipitates strengthened Cu–Zr alloys, J. Mater. Res. 30 (2) (2015) 248–256, https://doi.org/10.1557/jmr.2014.382.

[19] H.H. Li, S.H. Zhang, Y. Chen, M. Cheng, H.W. Song, J.S. Liu, Effects of small amount addition of rare earth Ce on microstructure and properties of cast pure copper, J. Mater. Eng. Perform. 24 (2015) 2857–2865, https://doi.org/10.1007/s11665-015-1595-x.

[20] Z.K. Guo, J.C. Jie, J.M. Liu, S.P. Yue, S.C. Liu, T.J. Li, Effect of cold rolling on aging precipitation behavior and mechanical properties of Cu–15Ni–8Sn alloy, J. Alloy. Compd. 848 (2020) 156275, https://doi.org/10.1016/j.jallcom.2020.156275.

[21] Y.J. Ban, Y.F. Geng, J.R. Hou, Y. Zhang, M. Zhou, Y.L. Jia, B.H. Tian, Y. Liu, X. Li, A.A. Volinsky, Properties and precipitates of the high strength and electrical conductivity Cu-Ni-Co-Si-Cr alloy, J. Mater. Sci. Technol. 93 (2021) 1–6, https://doi.org/10.1016/j.jmst.2021.03.049.

[22] Z. Rdzawski, W. Głuchowski, J. Stobrawa, J. Sobota, Effect of rare-earth metals addition on microstructure and properties of selected copper alloys, Arch. Metall. Mater. 59 (2) (2014) 641–648, https://doi.org/10.2478/amm-2014-0105.

[23] J.Y. Cheng, B. Shen, F.X. Yu, Precipitation in a Cu–Cr–Zr–Mg alloy during aging, Mater. Charact. 81 (Complete) (2013) 68–75, https://doi.org/10.1016/j.matchar.2013.04.008.

[24] M.R. Ahmadi, B. Sonderegger, E. Povoden-Karadeniz, A. Falahati, E. Kozeschnik, Precipitate strengthening of non-spherical precipitates extended in<100>or {100} direction in fcc crystals, Mater. Sci. Eng. A 590 (2014) 262–266, https://doi.org/10.1016/j.msea.2013.10.043.

[25] B. Sonderegger, E. Kozeschnik, Particle strengthening in fcc crystals with prolate and oblate precipitates, Scr. Mater. 66 (1) (2012) 52–55, https://doi.org/10.1016/j.scriptamat.2011.10.003.

[26] W.N. Liao, H.Q. Yang, C. Yi, J.H. Zheng, Effect and mechanism of cold rolling and aging process on microstructure and properties of columnar grain C70250 copper alloy, Mater. Sci. Eng.: A 833 (2022) 142577, https://doi.org/10.1016/j.msea.2021.142577.

[27] A. Bodyakova, R. Mishnev, A. Belyakov, R. Kaibyshev, Effect of chromium content on precipitation in Cu–Cr–Zr alloys, J. Mater. Sci. 57 (27) (2022) 13043–13059, https://doi.org/10.1007/s10853-022-07454-8.

[28] S. Nagarjuna, K. Balasubramanian, D.S. Sarma, Effect of prior cold work on mechanical properties and structure of an age-hardened Cu-1.5wt%Ti alloy, J. Mater. Sci. 32 (1997) 3375–3385, https://doi.org/10.1023/A:1018608430443.

[29] Y. Zhou, S. Zeng, H. Li, H.W. Zhang, H.F. Zhang, Z.W. Zhu, A design of Zr-rich body-centered cubic structured refractory complex concentrated alloy with outstanding tensile strength and ductility, Mater. Sci. Eng.: A 874 (2023) 145091, https://doi.org/10.1016/j.msea.2023.145091.

[30] S.G. Mu, F.A. Guo, Y.Q. Tang, X.M. Cao, M.T. Tang, Study on microstructure and properties of aged Cu–Cr–Zr–Mg–RE alloy, Mater. Sci. Eng.: A 475 (1-2) (2008) 235–240, https://doi.org/10.1016/j.msea.2007.04.056.

[31] A.H. Huang, Y.F. Wang, M.S. Wang, L.Y. Song, Y.S. Li, L. Gao, C.X. Huang, Y. T. Zhu, Optimizing the strength, ductility and electrical conductivity of a Cu-Cr-Zr alloy by rotary swaging and aging treatment, Mater. Sci. Eng.: A 746 (2019) 211–216, https://doi.org/10.1016/j.msea.2019.01.002.

[32] J. Su, Q. Dong, P. Liu, H. Li, B. Kang, Research on aging precipitation in a Cu–Cr–Zr–Mg alloy, Mater. Sci. Eng.: A 392 (1-2) (2005) 422–426, https://doi.org/10.1016/j.msea.2004.09.041.

[33] R. Mishnev, I. Shakhova, A. Belyakov, R. Kaibyshev, Deformation microstructures, strengthening mechanisms, and electrical conductivity in a Cu–Cr–Zr alloy, Mater. Sci. Eng.: A 629 (2015) 29–40, https://doi.org/10.1016/j.msea.2015.01.065.

[34] H. Fernee, J. Nairn, A. Atrens, Precipitation hardening of Cu-Fe-Cr alloys part I Mechanical and electrical properties, J. Mater. Sci. 36 (2001) 2711–2719, https://doi.org/10.1023/A:1017916930459.

[35] B.J. Wang, Y. Zhang, B.H. Tian, V. Yakubov, J. An, A.A. Volinsky, Y. Liu, K.X. Song, L.H. Li, M. Fu, Effects of Ce and Y addition on microstructure evolution and precipitation of Cu-Mg alloy hot deformation, J. Alloy. Compd. 781 (2019) 118–130, https://doi.org/10.1016/j.jallcom.2018.12.022.

[36] A.H. Huang, Y.F. Wang, M.S. Wang, L.Y. Song, Y.S. Li, L. Gao, C.X. Huang, Y. T. Zhu, Optimizing the strength, ductility and electrical conductivity of a Cu-Cr-Zr alloy by rotary swaging and aging treatment, Mater. Sci. Eng.: A 746 (2019) 211–216, https://doi.org/10.1016/j.msea.2019.01.002.

[37] P. Liu, B.X. Kang, X.G. Cao, J.L. Huang, H.C. Gu, Strengthening mechanisms in a rapidly solidified and aged Cu-Cr alloy, J. Mater. Sci. 35 (2000) 1691–1694, https://doi.org/10.1023/A:1004760014886.

[38] H.D. Fu, S. Xu, W. Li, J.X. Xie, H.B. Zhao, Z.J. Pan, Effect of rolling and aging processes on microstructure and properties of Cu-Cr-Zr alloy, Mater. Sci. Eng.: A 700 (2017) 107–115, https://doi.org/10.1016/j.msea.2017.05.114.

[39] G. Purcek, H. Yanar, O. Saray, I. Karaman, H.J. Maier, Effect of precipitation on mechanical and wear properties of ultrafine-grained Cu–Cr–Zr alloy, Wear 311 (1-2) (2014) 149–158, https://doi.org/10.1016/j.wear.2014.01.007.

[40] Q. Liu, X. Zhang, Y. Ge, J. Wang, J.Z. Cui, Effect of processing and heat treatment on behavior of Cu-Cr-Zr alloys to railway contact wire, Metall. Mater. Trans. A 37 (2006) 3233–3238, https://doi.org/10.1007/BF02586158.

[41] N. Gao, E. Huttunen-Saarivirta, T. Tiainen, M. Hemmilä, Influence of prior deformation on the age hardening of a phosphorus-containing Cu–0.61 wt% Cr alloy, Mater. Sci. Eng.: A 342 (1-2) (2003) 270–278, https://doi.org/10.1016/s0921-5093(02)00306-4.

[42] P. Liu, X.B. Kang, G.X. Cao, J. L, Aging precipitation and recrystallization of rapidly solidified Cu–Cr–Zr–Mg alloy, Mater. Sci. Eng.: A 265 (1-2) (1999) 262–267, https://doi.org/10.1016/S0921-5093(98)01149-6.

[43] H.Y. Yang, Z.C. Ma, C.H. Lei, L. Meng, Y.T. Fang, J.B. Liu, H.T. Wang, High strength and high conductivity Cu alloys: a review, Sci. China Technol. Sci. 63 (12) (2020) 2505–2517, https://doi.org/10.1007/s11431-020-1633-8.

[44] H. Suzuki, M. Kanno, I. Kawakatsu, Strength of Cu-Zr-Cr alloy relating to the aged structures, J. Jpn. Inst. Met. 33 (5) (1969) 628–633, https://doi.org/10.2320/jinstmet1952.33.5628.

[45] V.I. Zel'dovich, N.Yu Frolova, I.V. Khomskaya, A.E. Kheifets, Electron microscopic investigation of aging in the Cu–0.06% Zr alloy, Phys. Met. Metallogr. 117 (2016) 710–718, https://doi.org/10.1134/S0031918×1607019X.

[46] L. Arnberg, U. Backmark, N. Bäckström, J. Lange, A new high strength, high conductivity Cu-0.5 wt% Zr alloy produced by rapid solidification technology, Mater. Sci. Eng. 83 (1) (1986) 115–121, https://doi.org/10.1016/0025-5416(86)90178-3.

[47] T.M. Wang, M.Y. Li, H.J. Kang, Wei Wang, C.L. Zou, Z.N. Chen, Effects of trace La additions on the microstructures and properties of nanoprecipitates strengthened Cu–Zr alloys, J. Mater. Res. 30 (2) (2015) 248–256, https://doi.org/10.1557/jmr.2014.382.

[48] H. Fernee, J. Nairn, A. Atrens, Precipitation hardening of Cu-Fe-Cr alloys part I Mechanical and electrical properties, J. Mater. Sci. 36 (2001) 2711–2719, https://doi.org/10.1023/A:1017916930459.

[49] X.P. Xiao, H. Xu, J.S. Chen, Q.M. Liang, J.F. Wang, J.B. Zhang, Aging properties and precipitates analysis of Cu-2.3Fe-0.03P alloy by thermomechanical treatments,

Mater. Res. Express 4 (11) (2017) 116511, https://doi.org/10.1088/2053-1591/aa96d4.

[50] Y.J. Ban, M. Zhou, Y. Zhang, Y.L. Jia, Y. Pang, Y.Z. Li, S.L. Tang, X. Li, A. A. Volinsky, E.S. Marchenko, Abnormally high work hardening ability and excellent comprehensive properties of copper alloys due to multiple twins and precipitates, Mater. Des. 228 (2023) 111819, https://doi.org/10.1016/j.matdes.2023.111819.

[51] H. Watanabe, T. Kunimine, C. Watanabe, R. Monzen, Y. Todaka, Tensile deformation characteristics of a Cu− Ni− Si alloy containing trace elements processed by high-pressure torsion with subsequent aging, Mater. Sci. Eng.: A 730 (2018) 10–15, https://doi.org/10.1016/j.msea.2018.05.090.

[52] A.P. Zhilyaev, I. Shakhova, A. Morozova, A. Belyakov, R. Kaibyshev, Grain refinement kinetics and strengthening mechanisms in Cu–0.3Cr–0.5Zr alloy subjected to intense plastic deformation, Mater. Sci. Eng.: A 654 (2016) 131–142, https://doi.org/10.1016/j.msea.2015.12.038.

[53] Y.F. Geng, Z.Y. Zhang, K.X. Song, Y.L. Jia, X. Li, H.R. Stock, H.L. Zhou, B.H. Tian, Y. Liu, A.A. Volinsky, X.H. Zhang, P. Liu, X.H. Chen, Effect of Ce addition on microstructure evolution and precipitation in Cu-Co-Si-Ti alloy during hot deformation, J. Alloy. Compd. 842 (2) (2020) 155666, https://doi.org/10.1016/j.jallcom.2020.155666.

[54] Y.J. Ban, Y. Zhang, B.H. Tian, K.X. Song, M. Zhou, X.H. Zhang, Y.L. Jia, X. Li, Y. F. Geng, Y. Liu, A.A. Volinsky, EBSD analysis of hot deformation behavior of Cu-Ni-Co-Si-Cr alloy, Mater. Charact. 169 (1) (2020), https://doi.org/10.1016/j.matchar.2020.110656.

[55] A.S.H. Kabir, M. Sanjari, J. Su, I.H. Jung, S. Yue, Effect of strain-induced precipitation on dynamic recrystallization in Mg–Al–Sn alloys, Mater. Sci. Eng.: A 616 (2014) 252–259, https://doi.org/10.1016/j.msea.2014.08.032.

[56] C. Haase, L.A. Barrales-Mora, Influence of deformation and annealing twinning on the microstructure and texture evolution of face-centered cubic high-entropy alloys, Acta Mater. 150 (2018) 88–103, https://doi.org/10.1016/j.actamat.2018.02.048.

[57] Y. Chino, K. Kimura, M. Mabuchi, Twinning behavior and deformation mechanisms of extruded AZ31 Mg alloy, Mater. Sci. Eng.: A 486 (1-2) (2008) 481–488, https://doi.org/10.1016/j.msea.2007.09.058.

[58] M. Gholami, J. Vesely, I. Altenberger, H.-A. Kuhn, M. Janecek, M. Wollmann, L. Wagner, Effects of microstructure on mechanical properties of CuNiSi alloys, J. Alloy. Compd. 696 (2017) 201–212, https://doi.org/10.1016/j.jallcom.2016.11.233.

[59] Y.K. Wu, Y. Li, J.Y. Lu, S.T. Tan, F. Jiang, J. Sun, Correlations between microstructures and properties of Cu-Ni-Si-Cr alloy, Mater. Sci. Eng.: A 731 (2018) 403–412, https://doi.org/10.1016/j.msea.2018.06.075.